A study of measurement scenarios for the future CO2M mission: avoidance of detector saturation and the impact on XCO2 retrievals

Michael Weimer[1], Michael Hilker[1], Stefan Noël[1], Max Reuter[1], Michael Buchwitz[1], Blanca Fuentes Andrade[1], Rüdiger Lang[2], Bernd Sierk[2], Yasjka Meijer[3], Heinrich Bovensmann[1], John P. Burrows[1], and Hartmut Bösch[1]

[1]Institute of Environmental Physics, University of Bremen, Bibliothekstraße 1, 28359 Bremen, Germany
[2]EUMETSAT, EUMETSAT-Allee 1, 64295 Darmstadt, Germany
[3]European Space Agency, Keplerlaan 1, 2201 AZ Noordwijk, the Netherlands

Correspondence: Michael Weimer (mweimer@iup.physik.uni-bremen.de)

Abstract. The direct and indirect release ~~by humans~~ of carbon dioxide (CO_2) by human activities into the atmosphere is the main driver of the anthropogenic change in climate since the industrial revolution. The Paris agreement from 2015 requires regular country-based reports of greenhouse gas emissions. Inverse modeling of observed concentrations of greenhouse gases is one important approach to verify the reported emissions. The future constellation of Copernicus Anthropogenic CO_2 Monitoring (CO2M) satellites is dedicated to greenhouse gas measurements with high spectral and spatial resolution and wide coverage. The requirements for the performance of the instruments and retrieval algorithms for the column-averaged dry-air mole fraction (XCO_2) are stringent in order to identify, assess and monitor the CO_2 emissions from space. In this study, we analyze the impact of avoiding detector saturation on the precision and spatial coverage of XCO_2. We use the Fast atmOspheric traCe gAs retrievaL (FOCAL) algorithm which has been selected to be one of the operational greenhouse gas retrieval algorithms to be implemented within the CO2M ground segment. In order to avoid saturation, the number of read-outs per sampling time can be increased and the signals can be co-added onboard, which we refer to as "temporal oversampling" in this study. We use a subsampled one-year dataset of simulated radiances to define the temporal oversampling factors (OSFs) that are sufficient to avoid detector saturation and then apply the defined OSF combinations globally. We find that OSFs larger than one will lead to a significant decrease in number of saturated observations with some impact on the median XCO_2 precision, concluding that OSFs larger than one should be considered for the satellite mission. These results are based on simulated radiances. Consequently, the real impact on the precision should be analyzed in more detail during the commissioning phase of the satellite.

1 Introduction

It is now well established that the direct and indirect release of carbon dioxide ~~by humans~~ (CO_2) by human activities, since the industrial revolution, is the most important cause of the recent climate change (IPCC, 2023). Due to its long projected and irreversible impact on global warming on a timescale of a millennium (e.g., Archer et al., 2009; Solomon et al., 2009) and its sources from fossil fuel combustion among others, reduction of CO_2 emissions is an internationally agreed environmental

policy goal, as stated e.g. in the Paris Agreement from 2015 (UNFCCC, 2015). This agreement requires that countries report their emissions on a regular basis. Atmospheric measurements of the CO_2 concentrations, including e.g. in-situ surface observations and satellite-based remote sensing instruments, combined with inverse modeling to determine surface fluxes offer a unique opportunity to verify and support these reported emissions.

Space-borne total column CO_2 measurements have a long history starting with those retrieved from the pioneering instrument SCanning Imaging Absorption spectroMeter for Atmospheric CHartographY (SCIAMACHY, Burrows et al., 1995; Bovensmann et al., 1999; Buchwitz et al., 2005; Reuter et al., 2010; Schneising et al., 2011) and other satellites such as the Greenhouse gases Observing SATellite (GOSAT) and GOSAT-2 (Kuze et al., 2009; Nakajima et al., 2012), the Orbiting Carbon Observatory (OCO) version 2 and 3 (Crisp, 2015; Taylor et al., 2020) and TanSat (Liu et al., 2018).

The Copernicus Anthropogenic CO_2 Monitoring (CO2M) mission is a future constellation of three identical satellites in a near-polar sun-synchronous orbit with an equator crossing time at 11:30 LT in a descending node (Janssens-Maenhout et al., 2020; Sierk et al., 2021; Meijer et al., 2023). The first satellite is planned to be launched in ~~2026.~~ 2027. The mission builds on the concepts of CarbonSat with extended instrumentation (Bovensmann et al., 2010; Velazco et al., 2011; Buchwitz et al., 2013; Pillai et al., 2016; Broquet et al., 2018). Its primary instrument is a push-broom imaging spectrometer (CO2I) measuring solar radiances reflected at the Earth's surface and scattered in the atmosphere in three spectral bands: a) the near infrared (NIR, $747 - 773\,nm$), used to retrieve information about scattering properties and the atmospheric dry-air column density, aerosols and solar-induced fluorescence (SIF); b) and two bands in the short-wave infrared (SWIR1, $1590 - 1675\,nm$ and SWIR2, $1990 - 2095\,nm$), used to derive information about atmospheric CO_2, CH_4, aerosols and water vapor. As a result the satellites will enable the determination of the column-averaged dry-air mole fraction of atmospheric CO_2 and CH_4, called XCO_2 and XCH_4 hereafter, at a total spatial sample size of about $4\,km^2$ and a swath width of around $250\,km$. This resolution and swath width is a trade-off between detection of local sources and a frequent global coverage, with some limitations, e.g. due to clouds covering the tropospheric signal. In addition to CO2I, the CO2M mission will enable the measurement of the NO_2 content in the atmosphere with a spectrometer in the visible spectral range (NO2I), sharing the same slit, and information about clouds in the atmosphere with a Cloud Imager (CLIM) and about aerosols with a Multi-Angle Polarimeter (MAP), see also Meijer et al. (2023) for an overview.

The potential for CO_2 emission verification with CO2M has been shown by studies using simulated radiances (e.g., Kuhlmann et al., 2020) and using measurements of satellites already in operation (e.g., Reuter et al., 2019; Fuentes Andrade et al., 2024). Three retrieval algorithms are considered for the operational greenhouse gas product of CO2M with differences especially in the treatment of light scattering in the retrievals: the Remote sensing of Trace gas and Aerosol Product (RemoTAP, Lu et al., 2022), the Flexible and Unified Spectral InversiON ALgorithm Platform (Fusional-P-UOL-FP) based on the algorithm described in Cogan et al. (2012) and the Fast atmOspheric traCe gAs retrievaL (FOCAL, Reuter et al., 2017a, b; Noël et al., 2021, 2022, 2024).

Quantifying anthropogenic CO_2 emissions from space is challenging because atmospheric signals resulting from these emissions are usually less than $1\,\%$ larger than the background (global $XCO_{2,bg} \approx 419\,ppm$ in 2023, Copernicus Climate Change Service, 2024). In addition, the natural variability during the year is of similar order of magnitude (e.g., Forkel et al.,

2016). Therefore, the precision ($0.7\,\text{ppm}$ for CO2I) and accuracy requirements ($0.5\,\text{ppm}$ for CO2I) to the instrument calibration and retrieval algorithms are stringent (ESA, 2020). Consequently, all aspects influencing the precision of the retrieved XCO_2

60 have to be considered and analyzed carefully in order to meet these requirements. Precision values between 0.4 and $0.6\,\text{ppm}$ could be inferred from several retrieval algorithms for CO2M using one read-out per integration time step (Lu et al., 2022; Reuter et al., 2024). Noël et al. (2024) showed first performance assessments of the FOCAL version for CO2M with simulated radiances. Here, we consider the effect of detector saturation and investigate the impact of reducing the detector exposure time in the nadir configuration where the instrument's zenith angle is close to zero in order to contribute to the planning of the

65 commissioning phase for CO2M.

Detector saturation occurs when the number of photons collected by the detector is larger than the characteristic full well capacity (FWC), e.g. due to a bright surface like a desert. Saturation of the detectors results in several negative impacts, which lead to errors in the CO_2 retrieval. At signal levels above the FWC the detector typically exhibits strong non-linearity with quickly fading response towards saturation (e.g., Staebell et al., 2021, for the airborne instrument MethaneAIR). In addition,

70 saturation could affect subsequent measurements due to memory effects (Gaucel et al., 2023). Consequently, saturation-affected measurements have to be removed (Yoshida et al., 2011; Kataoka et al., 2017; Tian et al., 2018; Shi et al., 2021) and should generally be avoided. The GOSAT instrument has different gain modes to avoid detector saturation (Kataoka et al., 2017; Reuter et al., 2012; Taylor et al., 2022). In glint geometry over ocean, where the satellite's field of view is shifted towards the sun-glint spot, it has been found that saturation can affect the measurements and can be avoided by looking near the glint spot

75 but excluding it (Boesch et al., 2011; Eldering et al., 2012; Crisp et al., 2017). Saturation in general can also be avoided by reducing the exposure time of the detector, thereby increasing the maximum detectable radiance in that spectral band, but also impacting the retrieved XCO_2 precision (Nakajima et al., 2015; Grossmann et al., 2018; Staebell et al., 2021; Clavier et al., 2024). This is further discussed in Sect. 2.

The goal of this study is to define scenarios reducing the detector exposure time while maximizing the coverage and mini-

80 mizing the negative impact of saturation on the XCO_2 precision. For this, we use simulated radiances calculated at the CO2M spatial samples with added noise corresponding to the respective detector setting. After defining detector saturation and its relation to the reduction of the exposure time in Sect. 2, we describe the simulated radiances used in this study (Sect. 3). As a next step, we define scenarios to determine the detector exposure time needed in each spectral band (see Sect. 4), then apply these scenarios to simulated radiances and retrieve XCO_2 using the FOCAL algorithm (Sect. 5). The impact of the scenarios

85 on the global XCO_2 precision is discussed in Sect. 6. Section 7 provides some concluding remarks.

2   Detector design, saturation, oversampling factor, signal-to-noise ratio

The design of the CO2I/NO2I is comprised of four grating spectrometers sharing a common telescope, entrance slit and collimator, as described in Sierk et al. (2021). Here we briefly summarize the features that are relevant for the present study. The multi-band spectrometer operates according to the push-broom imaging principle: The entrance slit is projected onto the

90 Earth's surface, defining the swath width in the across-track (ACT) direction. The CO2I/NO2I design features a slit composed
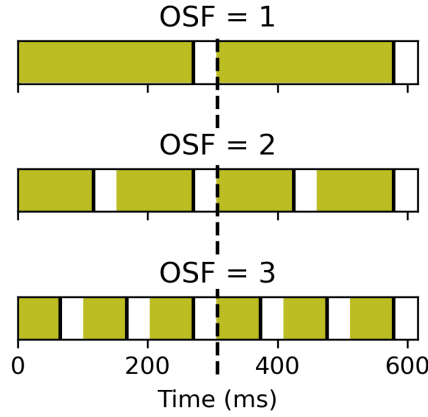
Figure 1. Illustration of the integration times (colored) for the oversampling factors that are foreseen for the detectors in the NIR and SWIR bands of CO2M. White spaces are times for reading out the signal (about $37\,\mathrm{ms}$). The end of the integration time is denoted by solid black lines at the end of each rectangle. Black dashed line: Sampling period t_{samp} of $308\,\mathrm{ms}$, see Eq. (2).

of a number of rectangular optical fibers, which are aligned to form an array of apertures defining the spatial samples. The fiber core dimensions define the spatial sample size in ACT direction ($326\,\mu\mathrm{m}$ corresponding to $1.8\,\mathrm{km}$ on Earth) and the instantaneous field-of-view (IFOV) in the along-track (ALT) direction ($124\,\mu\mathrm{m}$ corresponding to $814\,\mathrm{m}$ on Earth). The spatial sampling in ALT direction is performed by the motion of the IFOV during the integration period t_{int}, in which signal is accumulated on the detectors.

95 The timing of the CO2I/NO2I instrument is driven by the requirements for (a) spatial sampling ($\leq 4\,\mathrm{km}^2$) and (b) SNR of the spectral radiance measurement, see also Appendix C for a more detailed discussion. The ACT spatial sampling distance is given by the design of the slit homogenizer (as well as detector size and optical magnification), and is fixed to $1.8\,\mathrm{km}$. This allows for a maximum of $\sim 2.2\,\mathrm{km}$ spatial sampling distance in ALT. At the CO2M orbit this amounts to a sampling time 100 t_{samp} of about $308\,\mathrm{ms}$. Shorter sampling periods will lead to a reduction of the SNR that is most probably non-compliant with the requirements which is why the value of $308\,\mathrm{ms}$ is used in this study. A spatial sample therefore has the extent of about $1.8 \times 2.2 \approx 4\,\mathrm{km}^2$ (with small variation across the swath due to projection on the Earth's surface). At any instant in time, the detector pixels sample the image spatially in ACT direction and spectrally in the perpendicular direction. From the signal of the dispersed light (in electrons), integrated during the sampling period, radiance spectra are derived, one for each fiber comprising 105 the entrance slit.

The number of electrons accumulated by a detector pixel sampling the wavelength λ, denoted as signal $S(\lambda)$, depends on the ground scene as well as the properties of the spectrometer, and can be as expressed as:

$$S(\lambda) = L(\lambda) \cdot \eta \cdot \tau \cdot \Delta\lambda \cdot QE(\lambda) \cdot t_{\mathrm{int}} \qquad (1)$$

Here, $L(\lambda)$ is the top-of-atmosphere spectral radiance, η the étendue of the instrument (product of entrance pupil area and 110 observation solid angle), τ the transmission of the optics, $\Delta\lambda$ the spectral bandwidth (or sampling interval) of the pixel, and

QE the quantum efficiency of the detector. t_{int} is the time during which light is accumulated within the sampling period. It has been decided to operate CO2I's SWIR detectors in "Integration Then Read" mode, in order to minimize bias effects from the detector's read-out electronics. In this mode, the signal of every acquired frame has to be completely read out before a new acquisition is started. During the read-out time t_{RO} of about $37\,\mathrm{ms}$, the signal integration is paused. Accordingly, t_{int} as such is reduced by multiples of t_{RO}:

$$t_{\mathrm{int}} = t_{\mathrm{samp}} - \mathrm{OSF} \cdot t_{\mathrm{RO}} \tag{2}$$

The factor OSF denotes the temporal oversampling factor, which is the number of detector read-outs within the sampling time. An illustration of the integration times for different OSFs can be found in Fig. 1. Multiple read-outs (OSF > 1) become necessary when the number of electrons accumulated during integration time exceeds the FWC of the detector pixels (called saturation hereafter). Note that the gaps in signal integration indicated by the white spaces in Fig. 1 are short with respect to the sampling time. They do not result in spatial under-sampling as the IFOV in ALT direction (approx. $800\,\mathrm{m}$) is larger than the on-ground motion of the entrance slit image during the read-out time, which is about $200\,\mathrm{m}$. An OSF larger than one increases the maximum radiance that can be measured by the detector, which is proportional to the time of each individual integration time (colored in Fig. 1).

The detectors used for the NIR detector (Teledyne-E2V) and the two SWIR spectrometers of CO2I/NO2I (Lynred NGP) feature a FWC of approximately 61.000 and 650.000 electrons, respectively. If the signal acquired during integration time exceeds this limit, the respective detector pixel becomes saturated. Such pixels do not yield meaningful measurements and tests showed that if saturation occurs it usually does not happen only at one spectral detector pixel but for more than $3\,\%$ of the pixels with the largest signal. Therefore, it can be expected that a large fraction of the continuum range of the spectrum is affected by saturation so that the measurement is not useful for the retrieval and a radiance spectrum with saturated pixels has to be discarded. In order to avoid data loss, the detector can however be operated with OSF > 1, meaning that more than one read-out cycle is performed within the sampling period of $t_{\mathrm{samp}} = 308\,\mathrm{ms}$ (Fig. 1). The value of $308\,\mathrm{ms}$ was used to meet all demands within the mission requirements. Apart from data loss over bright ground scenes, the necessity for saturation avoidance by temporal oversampling (OSF > 1) arises from the inherent effect of instrument stray light. Efficient correction of stray light from imperfect optical components (surface roughness and contamination), as well as parasitic reflections between them (ghosts) is mandatory to achieve compliance with the stringent radiometric requirements of the CO2M mission. Stray light correction algorithms require accurate knowledge of the signal distribution across the focal plane, which is derived from the measured signal image. In the presence of signal saturation, and hence invalid radiation measurements, such correction becomes inaccurate, if not infeasible, since the largest stray light contribution from the brightest signals cannot be reconstructed. For the reasons outlined above, the CO2I/NO2I spectrometer is likely to be operated with temporal oversampling, leading to signal loss according to Eq. (2). In the main part of this study, we neglect the effect of saturation on neighboring spatial samples in the swath and memory effects and remove spatial samples in case of saturation in their spectrum.

A major drawback of oversampling is the loss of radiometric signal from the total read-out time $\mathrm{OSF} \cdot t_{\mathrm{RO}}$, which decreases the signal-to-noise ratio (SNR) because the read-out noise increases with mutliple read-outs. In order to quantify the impact

of oversampling on SNR we further develop Eq. (1) to obtain an expression for the signal-to-noise ratio of the measured radiances: The shot noise of the measurement, given by the square root of the signal $S(\lambda)$ combines with the signal-independent components of the detection as

$$N_{\text{total}} = \sqrt{S(\lambda) + (I_{\text{dark}} + I_{\text{Tb}}) \cdot t_{\text{int}} + (N_{\text{RO}}^2 + N_{\text{AD}}^2 + N_{\text{VC}}^2) \cdot \text{OSF}}, \tag{3}$$

where I_{dark} is the dark current of the detector, I_{Tb} the shot noise from background thermal emission, N_{RO} its read-out noise, N_{AD} the digitization noise, and N_{VC} the video chain noise. The SNR can then be expressed as

$$\text{SNR} = \frac{A \cdot L}{\sqrt{A \cdot L + B}}, \tag{4}$$

in which the contributing noise sources are grouped into components scaling with the radiance $L(\lambda)$ and read as

$$A = \eta \cdot \tau \cdot \Delta\lambda \cdot QE(\lambda) \cdot [t_{\text{samp}} - (\text{OSF} \cdot t_{\text{RO}})], \tag{5}$$

and signal-independent parameters determined by the detector and read-out-electronics

$$B = (I_{\text{dark}} + I_{\text{Tb}}) \cdot [t_{\text{samp}} - (\text{OSF} \cdot t_{\text{RO}})] + (N_{\text{RO}}^2 + N_{\text{AD}}^2 + N_{\text{VC}}^2) \cdot \text{OSF}. \tag{6}$$

As can be seen, both the ~~nominator~~ numerator and denominator in Eq. (4) are affected when the oversampling factor is increased: The signal is decreased by the multiple read-out times, in which no signal electrons are integrated, and the total noise is increased, as more read-out noise is accumulated. Both effects reduce the SNR of the measured radiance for OSF > 1.

In order to apply the different OSF scenarios to the radiances, we use A and B parameters provided to us by ESA (ESA, private communication, 2023) to compute the SNR in the data using Eq. (4). In the files, these parameters are given for an edge spatial sample and a center spatial sample at discrete integer wavelengths so that they have to be interpolated to all detector pixels. We used linear interpolation in both wavelength and across-track dimensions. The A and B parameters depend on the number of read-outs and thus on the used OSF so that the SNR is OSF-specific at each wavelength.

Optimization of in-flight operation calls for avoidance of saturation on the one hand, while maintaining the largest possible SNR of the measured radiance spectra on the other. This optimization requires a careful analysis of the expected radiance levels and their variation, based on the realistic simulation of ground scenes, which is the topic of this study.

3   Radiance spectra simulated with SCIATRAN

We base our investigations on simulated radiances at the CO2M spatial samples, which we use as input for the retrievals. With simulated radiances, we have exact control over the noise that is added to the radiances so that the impact of increasing the OSF can be separated from other instrumental effects. The same one-year subset radiances, simulated with the SCIATRAN radiative transfer model are used as described by Noël et al. (2024). Here, we provide a brief summary of the dataset.

For this dataset, eight ACT (approximately every fifteenth) and every twentieth ALT spatial samples with solar zenith angles (SZAs) smaller than $80°$ (consistent with ESA, 2020) were selected using CO2M orbit data of one year provided

by EUMETSAT to simulate nadir radiances over land at these CO2M spatial samples with SCIATRAN (Rozanov et al., 2017).

175 The subset is chosen to reduce computation time while keeping an annual dataset and representatively sampling the geophysical conditions. The SCIATRAN radiative transfer model can be used to simulate radiative transfer through the Earth's atmosphere, including multiple scattering, in a wide range of wavelengths. For the generation of the dataset for this study, input pressure, temperature, clouds and water vapor profiles have been taken from the ECMWF re-analysis version 5 (ERA5, Hersbach et al., 2020) and other trace gas profiles as well as input parameters for the simulation of aerosols are taken from the Copernicus

180 Atmosphere Monitoring Service (CAMS, Inness et al., 2019) re-analysis data, both from the reference year 2015. The surface reflectivity needed to calculate the radiances have been derived using satellite measurements of the Moderate Resolution Imaging Spectroradiometer (MODIS). The simulation of solar chlorophyll fluorescence is based on Rascher et al. (2009). The simulations are restricted to scenes over land in the nadir mode of CO2M. Further details can be found in Noël et al. (2024).

4   Defining scenarios avoiding detector saturation

185 The goal of this section is to determine the maximum radiance in each spectral band and compare it with the OSF-specific saturation limit in order to estimate the OSF needed to avoid saturation. While different OSFs could be used along one orbit, switching would make mission operations more complex and may lead to other challenges such as OSF-dependent calibration (cf., Kataoka et al., 2017). Here, we investigate whether it is possible to use constant OSF settings all over the globe.

The left column of Fig. 2 shows the spectral and temporal maximum radiance occurring during the 1-year dataset of sim-

190 ulated radiances. They are binned to a 0.4x0.4 degree grid which corresponds roughly to the distance of every 15th spatial sample of CO2I/NO2I on the Earth's surface. As expected due to the solar irradiance spectrum, radiances are larger in the NIR than in the SWIR bands. Largest maximum radiances are simulated over the desert regions like the Sahara and the Australian deserts, especially in the SWIR bands which are sensitive to different surface types (e.g., Fasnacht et al., 2019; Manakkakudy et al., 2023; Santamaría-López et al., 2024). Increases also occur over the tropical rain forests due to the red-edge of plants

195 (e.g., Ge et al., 2019; Zeng et al., 2021). The ice-covered surface of Greenland shows increases in NIR and small values in the SWIR bands.

The color scales in Fig. 2 also include the radiance limits for the OSFs in each band. The global maximum radiance in NIR and SWIR1 correspond to values exceeding the limit of saturation for OSF 1, indicating that OSF > 1 might be needed to avoid saturation. The right column of Fig. 2 shows which OSF is sufficient in each grid box. The limit for OSF 1 is exceeded

200 over most parts of the land surface in the NIR band. In SWIR1, the latitude regions roughly between 30° N/S that include the tropical forests and deserts are also exceeding the saturation limit for OSF 1. The only region where an OSF of 3 is needed in the SWIR1 band is in the middle of Sahara where no significant anthropogenic sources of greenhouse gases exist. Therefore, OSF 1 and 2 are the dominant OSFs that are sufficient for SWIR1. In SWIR2, only some of the deserts show exceedance of the limit for OSF 1 where then OSF = 2 would be necessary to avoid saturation.

205 Table 1 shows the global fraction of spatial samples in the one-year subset dataset where the shown OSF is needed to avoid saturation. As can be seen, about 7 % of all spatial samples within the simulated year exceed the threshold for OSF 1 in the NIR
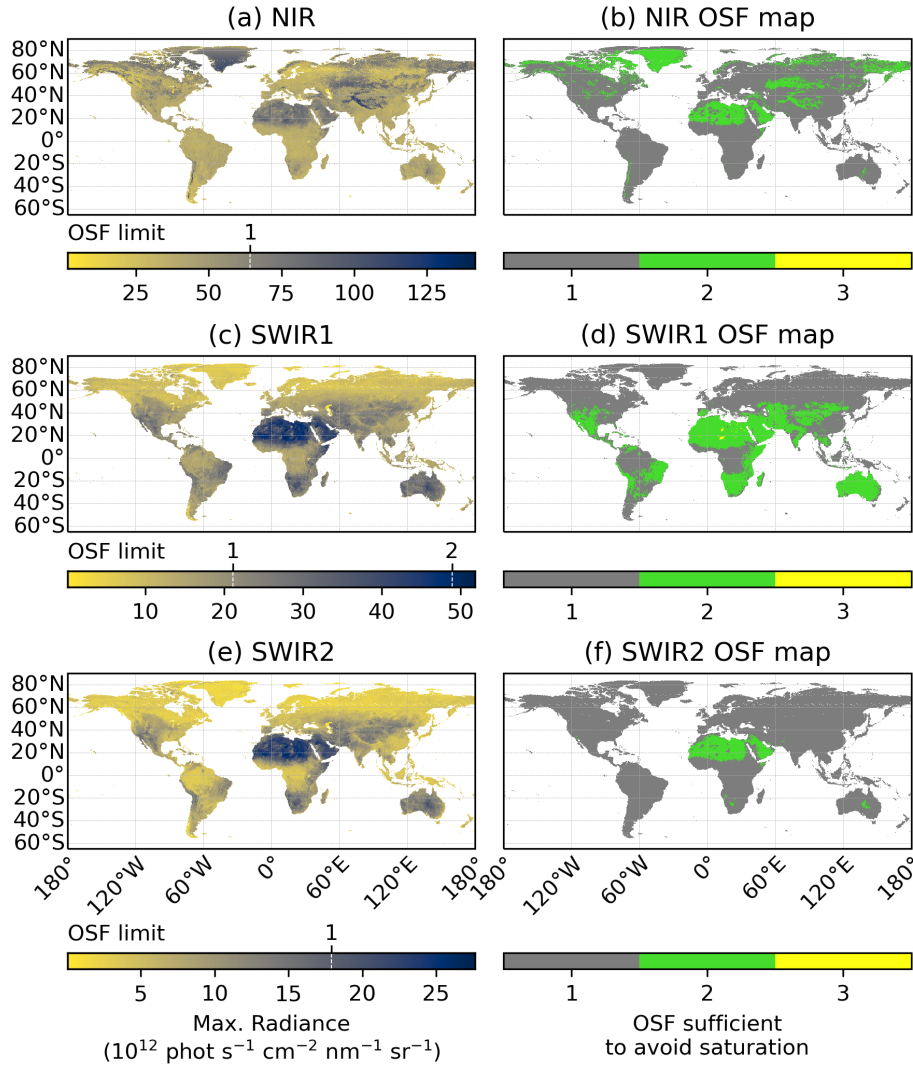
Figure 2. Left column: spectral and temporal maximum radiance in the simulated 1-year subset nadir radiances, binned to a 0.4x0.4 degree latitude-longitude grid. Clouds are removed for this analysis. The radiance limits corresponding to the OSFs in each wavelength band are illustrated by white dashed lines in the color scales of the panels. Right column: OSF needed in order to avoid saturation for the maximum radiances. The rows show the wavelength bands of CO2I: a, b NIR; c, d SWIR1 and e,f SWIR2. The simulated radiances are for nadir over land, only. Therefore, the ocean is masked by white color.

band. Although some spatial samples showed exceedance of the threshold for $OSF = 2$ in the NIR band (Fig. 2), the actual fraction in the whole one-year dataset is negligible. In the SWIR1 band, about $24\,\%$ of all spatial samples require $OSF = 2$. The locations requiring an OSF of three (yellow in panel d of Fig. 2) correspond only to a minor fraction of $0.04\,\%$. As expected from the previous analysis, the fraction for OSF of two is smaller for SWIR2 than for SWIR1 with a value smaller than $6\,\%$.

Table 1. Fraction of cloud-free spatial samples (in %) for which the radiance is between the saturation limits of OSF and OSF minus one in the 1-year dataset of simulated radiances.

OSF	NIR	SWIR1	SWIR2
1	93.01	75.81	94.36
2	6.99	24.15	5.64
3	0.00	0.04	0.00

Table 2. Oversampling factor (OSF) scenarios for the spectral bands of CO2M with their notation in this study. These OSFs are assumed to be applied globally in this study, details see text.

Notation	OSF_{NIR}	$\text{OSF}_{\text{SWIR1}}$	$\text{OSF}_{\text{SWIR2}}$
111	1	1	1
222	2	2	2
232	2	3	2
333	3	3	3

Therefore, a significant fraction of spatial samples exist that are affected by saturation with $\text{OSF} = 1$ in all bands so that OSFs larger than one should be further investigated which is the subject of this study. As the main fraction of saturated spatial samples are located over regions that are not known for large emission CO_2 sources, like over deserts and snow, we consider the OSF scenario $\text{OSF} = 1$ in all wavelength channels not only as a reference but also as one of the likely scenarios for CO2M. In addition, scenarios with $\text{OSF} = 2$ in all channels is considered in this study. As we use only a sub-sampled dataset for the global analysis we also add an OSF scenario with OSFs of 2 (NIR), 3 (SWIR1) and 2 (SWIR2) and a scenario with an OSF of 3 in all bands in case the missing spatial samples show larger radiances. The scenarios are summarized in Table 2 and denoted as OSF 111, 222, 232 and 333, respectively.

5 The FOCAL greenhouse gas retrieval algorithm

In this study, we use the updated version 1.1 of FOCAL-CO2M which is similar to the version used by Noël et al. (2024) with minor updates of coding optimizations. Therefore, we provide a brief summary of FOCAL here, with further details to be found in Noël et al. (2024) and references therein.

FOCAL is a radiative transfer and trace gas retrieval code approximating scattering in the atmosphere by a single scattering layer whose height, optical thickness and Ångström exponent are retrieved as part of the algorithm using optimal estimation. This approximation leads to an analytic expression for the calculation of scattering (Reuter et al., 2017b) making FOCAL a fast algorithm for the inversion of greenhouse gas concentrations from spectral measurements in the NIR and SWIR. FOCAL has been successfully applied to many satellites measuring greenhouse gases, such as OCO-2 (Reuter et al., 2017a, b) and GOSAT

and GOSAT-2 (Noël et al., 2021, 2022), and is one of the three operational algorithms to retrieve greenhouse gases from the future CO2M mission.

230 The FOCAL algorithm comprises pre-processing (i.e. filtering of measurements with bad quality and difficult scenes such as high SZAs), inversion and forward model (i.e. optimal estimation with an iterative approach starting with a-priori knowledge) and post-processing (i.e. convergence and variance filtering and bias correction). The setup of these steps here is similar to that used by Noël et al. (2024), which is why we refer to this publication for the details and describe here the adaptions made for this study.

235 As the noise model and the post-processing are specific to the setup of the instrument, e.g. the OSF, and we assume the application of one OSF scenario all over the globe, we use different noise models and post-processing for each OSF scenario. The post-processing uses a variance minimization process and filters data that have the largest impact on the scatter of the difference to the truth so that, in average, the differences to the truth are minimized. This means that variables and their limits to minimize the variance differ between the OSF scenarios, while keeping the total fraction of measurements that are removed,

240 which makes the OSF scenarios comparable to each other. Note that post-processing is based on 10% of the whole year's data. The setup of the noise model and the post-processing can be found in Appendix A.

In this study, we apply FOCAL-CO2M version 1.1 to the one year of simulated subset nadir radiances over land, filtered for clouds, a SZA larger than $75°$ and saturation, and retrieve XCO_2 using the OSF scenarios of Table 2. The impact on XCO_2 is discussed in the following section.

245 We will use the retrieval's random noise error arising from the different components discussed in Sect. 2 to investigate the impact on the XCO_2 precision. In addition, we will analyze the retrieval's smoothing error, which arises from the smoothing of the state connected to the averaging kernels (Rodgers, 2000), in combination with the noise error to make statements about the impact on the overall noise error. Remaining systematic errors after post-processing due to the different OSF settings should be small because the post-processing is calculated individually for each OSF scenario and will be analyzed in terms of overall

250 standard deviations of the retrieval residuals.

6 Impact of increasing the OSF

6.1 Impact on SNR

We first analyze how the SNR of the continuum radiance is affected by an increased OSF. Figure 3 shows the reduction of the SNR compared to $OSF = 1$ for the three spectral bands. While the maximum SNR for $OSF = 1$ is about 1000 in the NIR and

255 1600 in the SWIR bands, it is smaller for larger OSFs. For large SNRs, i.e. large radiances, A dominates Eq. (4) leading to a constant slope in all cases. The non-linear part corresponding to B leads to changes of the slope at the lower end of SNRs so that all lines converge to the origin. Ratios of SNR to OSF 1 are printed for each spectral band and are between 67 and 92% for $OSF = 2$ and between 47 and 83% for $OSF = 3$, see Fig. 3.

In the next step, we investigate the impact of the SNR changes, made in the previous analysis, on the retrieved a posteriori

260 noise of FOCAL. This could be used in the future to estimate the XCO_2 precision with the knowledge of the SNR change. In
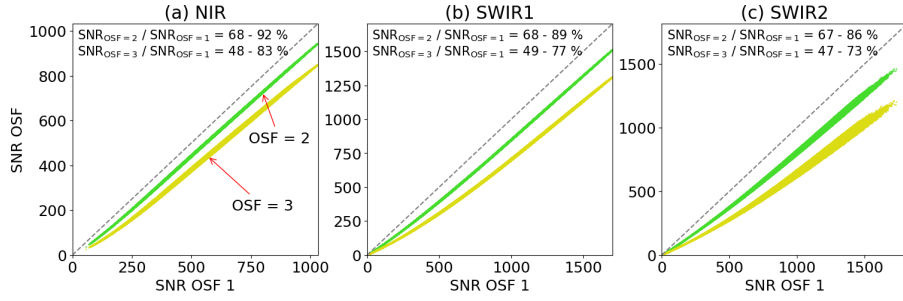
Figure 3. Signal-to-noise ratios compared to an OSF of one in (a) the NIR, (b) the SWIR1 and (c) the SWIR2 bands. The black dashed line illustrates the one-to-one line. In addition, the minimum and maximum of the ratio between the SNR to SNR for $OSF = 1$ is labeled in each panel for each OSF.

the easiest case, relative changes of the SNR (Φ) are proportional to relative changes of the a posteriori noise error (N), which can be written as

$$\frac{dN}{N} = C\frac{d\Phi}{\Phi} \tag{7}$$

with C as constant translating SNR changes to changes in XCO_2 a posteriori noise, i.e. precision. This assumption is tested in this section. Integrating Eq. 7 yields

$$\ln N = C \cdot \ln(\Phi) + k, \tag{8}$$

where k is an integration constant and the knowledge that N and Φ are positive numbers has been applied.

Equation 8 describes a linear relationship between N and Φ in a double-logarithmic space. It has been tested for all scenarios and bands which are shown in Fig. 4. This figure shows histograms of binned logarithmic SNR and a posteriori noise error values with linear regressions as dashed lines and formulas in the respective legends. The assumption of linearity does not apply to the NIR band because some high SNR values also have a large noise error because radiances in the NIR band are less sensitive to changes of CO_2 (only indirectly due to the dependence of the retrieved XCO_2 on atmospheric scattering and on the air column or surface pressure) than in the other bands. On the other hand, there is a clear linear relationship in the two SWIR bands. While the slopes of the regression lines differ among the OSF scenarios the negative values are largest in the NIR (average -0.69), smaller in SWIR1 (average -0.62) and smallest in SWIR2 (average -0.45). The smaller slope in SWIR2 compared to SWIR1 can probably be explained by the different number of spectral detector pixels in the CO_2 absorption region within the FOCAL fit windows: about 473 in SWIR1 and 770 in SWIR2 which makes single noisy measurements less sensitive to changes in XCO_2 in SWIR2. In addition, the sensitivity of the absorption lines to CO_2 changes are different in SWIR1 and SWIR2.

In summary, the SWIR2 band is less sensitive to changes in the SNR than SWIR1 where both the double-logarithmic linear relationship could be confirmed. Apart from values with high SNR and large noise for which the assumption of linearity does
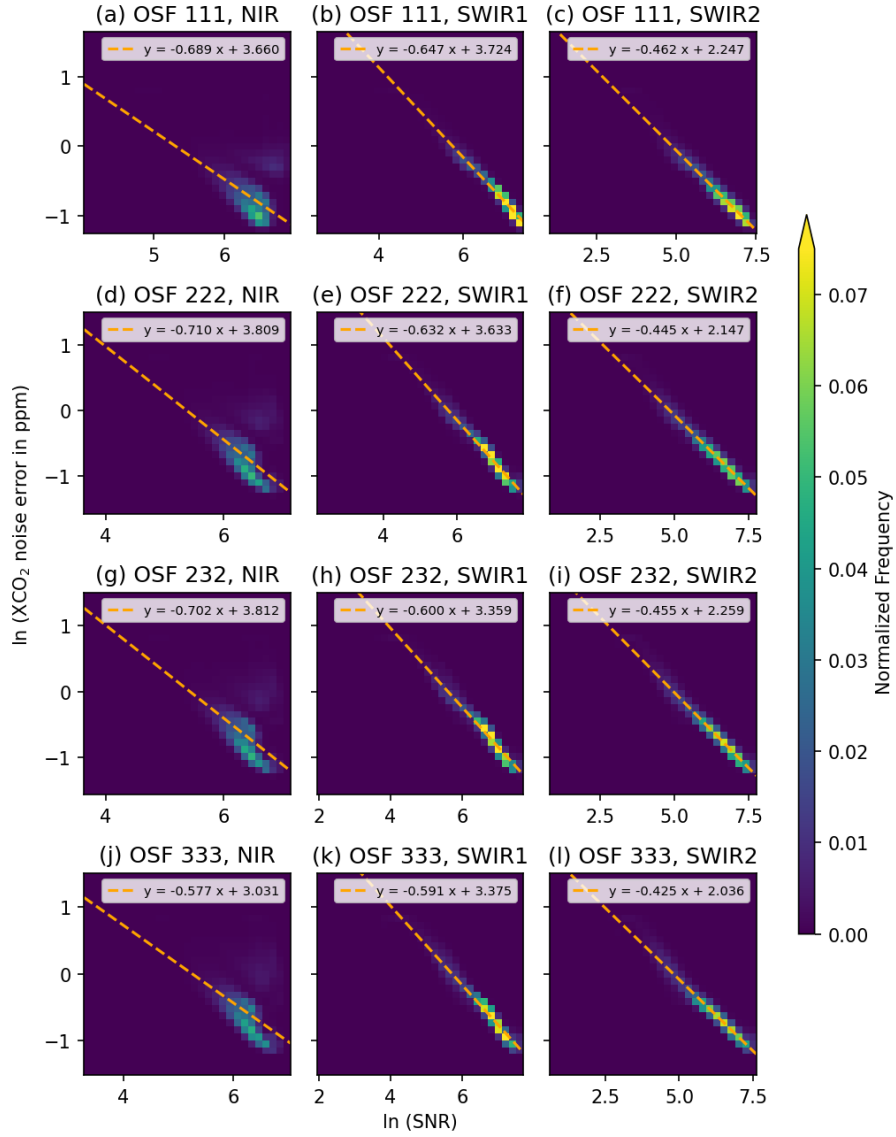
Figure 4. Logarithm of the continuum SNR versus logarithm of the FOCAL XCO_2 a posteriori noise error for all combinations of OSF scenarios and wavelength bands. Orange dashed lines show linear regressions for each panel with its parameters in their legend. Note the different values on the x-axes of each panel.

not hold, the slope in the NIR band is similar to that in the SWIR1 band, suggesting that the NIR band is of similar importance for the retrieval of XCO_2.
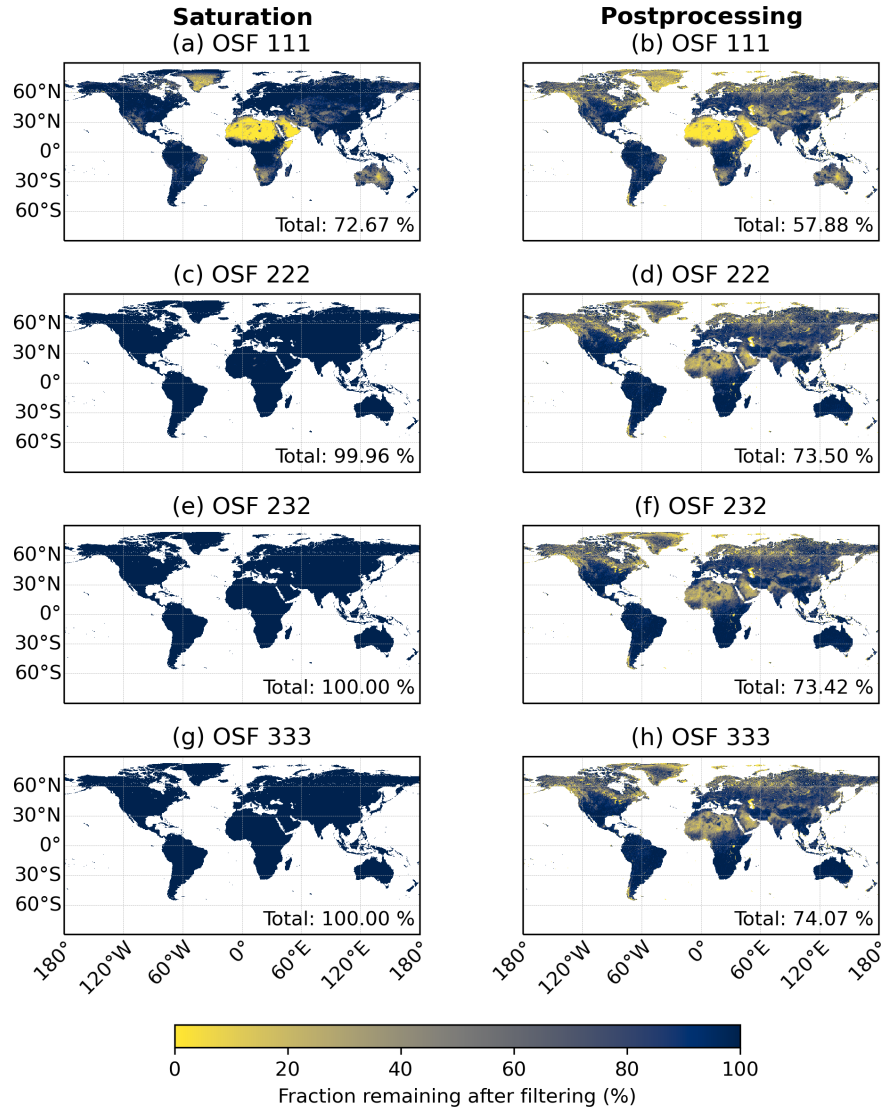
Figure 5. Throughput of the saturation filter during pre-processing (left column) and after post-processing (right column).The data are binned to a 0.4x0.4-degree latitude-longitude grid based on the CO2M spatial sample center coordinates. Note that the saturation filter is applied as the last filter and $100\,\%$ means the data after filtering for $SZA > 75°$ and cloud fraction > 0.2. The global fraction of remaining data is labeled as "Total" in the panels. The filters applied during post-processing can be found in Table A1 of Appendix A.

6.2 Impact on spatial coverage

285 As discussed in Sect. 2, spectra including saturated measurements have to be discarded, which will reduce the spatial coverage on Earth. In order to analyze the impact of filtering for saturation, the simulated radiances are binned to a 0.4x0.4-degree

latitude-longitude grid and the fraction of remaining data is shown in the first column of Fig. 5. As discussed above, the desert regions have large reflectances that will lead to saturation for all measurements in OSF 111 (panel a) e.g. over the Saharan region, the Arabian Peninsula and the deserts in Australia. Note that important emissions from oil and gas industry on the Arabian Peninsula would have to be filtered out when using OSF 111. In addition, the surface covered by ice such as Greenland and the Himalayas are filtered out as a result of saturation using OSF 111. In total, a fraction of 72.7% remains globally when adding an additional pre-processing filter for saturation in OSF 111. Because of possible stray light effects, we also did the analysis with removing whole swaths instead of single spatial samples, which can be found in Appendix B, and where a fraction of 47.3% remains after filtering for saturation.

As expected from the analysis of Sect. 4, increasing the OSF to values larger than one leads to better coverage. For instance, with OSF 222 (panel c), saturation only occurs at localized spots on the Sahara leading to an overall remaining fraction of data larger than 99%. For the scenarios with larger OSFs (232 and 333), 100% of the values remain, i.e. no saturation or saturation in the sub-% range is simulated in these cases. On the other hand, the majority of locations affected by saturation are in regions where no significant emission sources exist so that OSF 111 could still be sufficient for the goal of estimation of localized emission sources.

Another aspect is post-processing which filters parts of the data, independent of saturation, and the fraction of data remaining after saturation filter and post-processing is shown in the second column of Fig. 5. The filters applied during post-processing depend on the scenario and can be found in Table A1 of Appendix A. While the post-processing filters part of the data over the Sahara and the Arabian Peninsula also for $OSF > 1$, data are additionally lost at the high latitudes. The patterns are similar for all OSF scenarios. In total, about 58% are left for OSF 111 and about 73% for the other scenarios.

6.3 Impact on XCO_2

While the overall coverage increases with OSFs larger than one the precision is reduced due to read-out noise. We determine the impact on the precision by calculating FOCAL's a posteriori XCO_2 retrieval noise. Histograms of the a posteriori error (which is the root sum squares of the noise and smoothing errors), noise error and the difference of retrieved XCO_2 minus a priori (equal to true) XCO_2 for the whole one-year dataset and all OSF scenarios of Table 2 are shown in Fig. 6. All panels include median, $q_{0.5}$, and standard deviation, σ, of the respective histogram. Both a posteriori error and noise error increase with larger OSFs. For OSF 333 errors are estimated to be a factor of about 1.2 larger than the OSF 111 errors in the median. For OSF 222, this factor is 1.06. Note that this value refers to the median noise and can be larger for single measurements, see distributions of middle column in Fig. 6. A discussion where the impact on precision is largest for the respective OSF scenarios follows later in this section. In addition, the variance, which is the square of these values, is connected to the information reduction, which is 39% for OSF 333 and 12% for OSF 222, compared to OSF 111.

The median of the a posteriori error is $0.56\,\mathrm{ppm}$ for OSF 111 compared to a $0.44\,\mathrm{ppm}$ noise error and similar for the other OSF scenarios. Therefore, the error of XCO_2 is dominated by the noise component of the error induced by changing the OSF in each scenario.
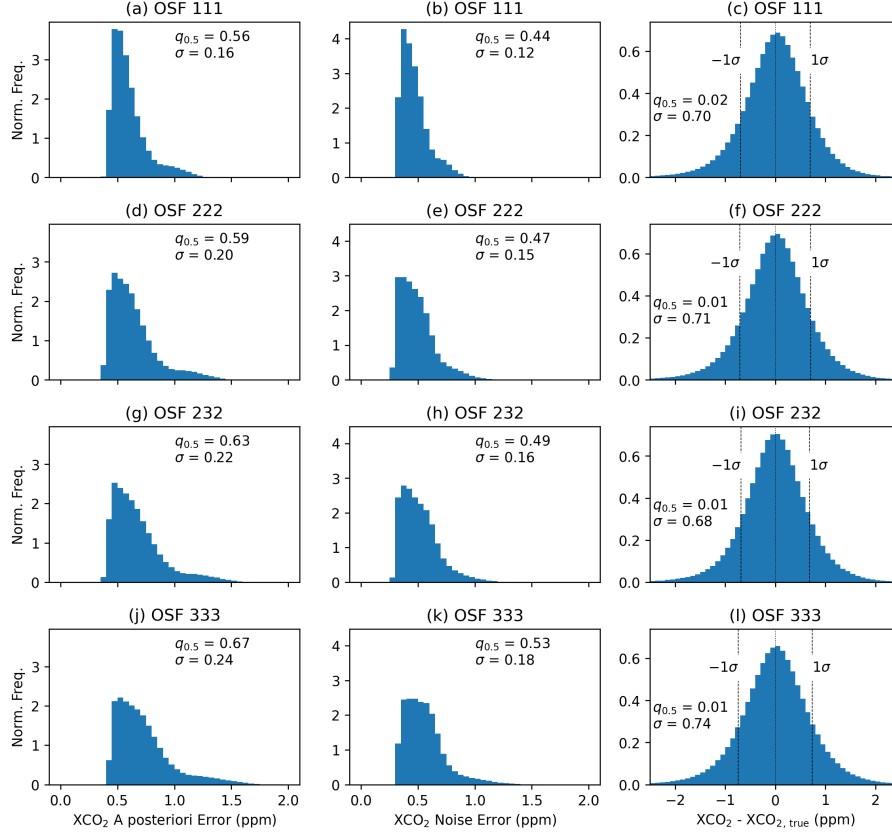
Figure 6. Histograms of the global distribution of the a posteriori XCO_2 retrieval error (first column), the a posteriori XCO_2 noise error (second column) and the differences between FOCAL XCO_2 after post-processing and the true XCO_2 (third column) for the whole year of simulated subset radiances. The rows show OSF 111, 222, 232 and 333, respectively. Median ($q_{0.5}$) and standard deviation (σ) of the distributions are added to each panel in units of ppm. Note that the standard deviation of $XCO_2 - XCO_{2,\text{true}}$ includes both systematic and random noise contributions.

As expected from adapting the post-processing to each OSF scenario, the distributions of $XCO_2 - XCO_{2,\text{true}}$ in the right column of Fig. 6 are nearly symmetric around $0\,\text{ppm}$, as demonstrated by median values close to zero. Note that the post-processing is based on $10\,\%$ of all available data. Due to slightly larger noise errors for OSF > 111, the standard deviations increase slightly from $0.70\,\text{ppm}$ for OSF 111 to $0.74\,\text{ppm}$ for OSF 333. Note that this value includes both systematic and random errors that were not separated in this analysis, as e.g. in Noël et al. (2024).

The OSF scenarios 111 and 222 show an increase of median noise errors in the order of $0.03\,\text{ppm}$ so that the decrease in global XCO_2 precision is estimated to be small in the setup of this study.
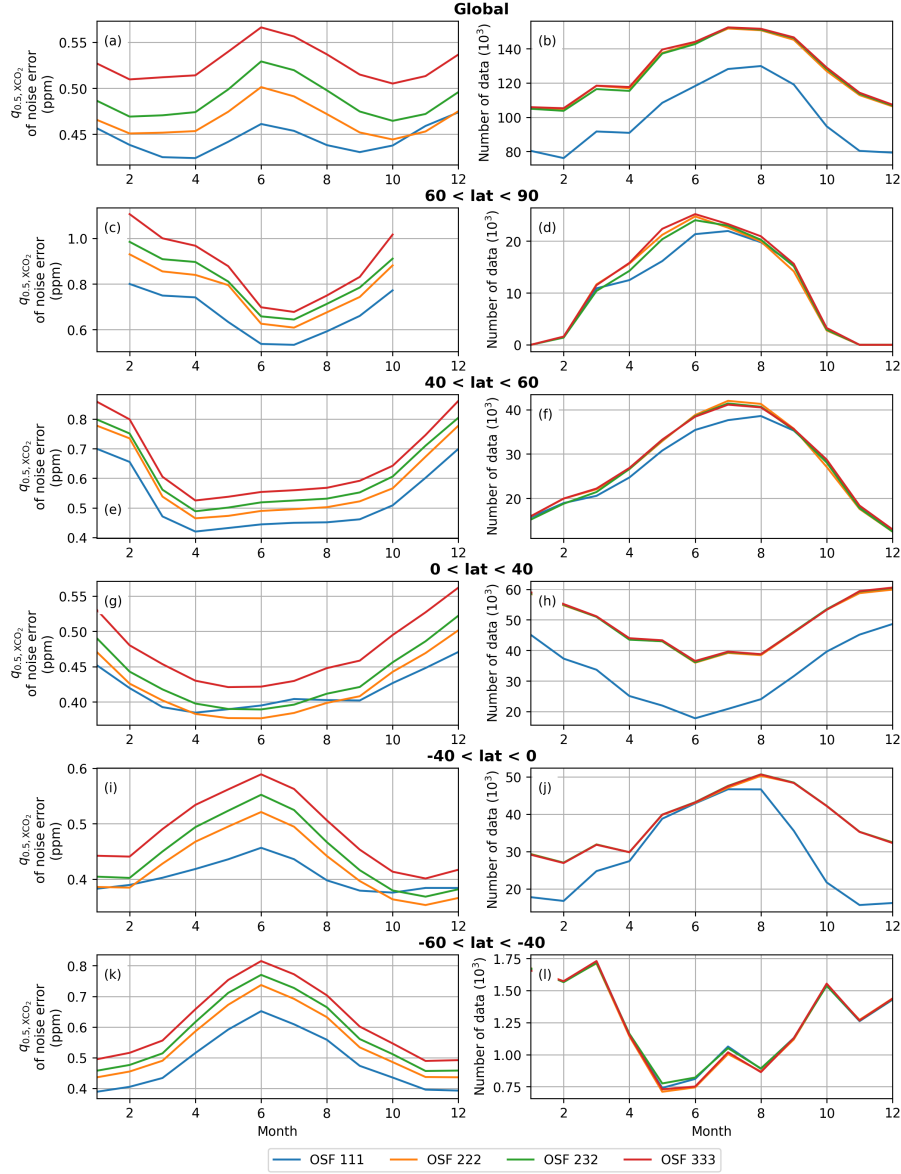
Figure 7. Timeseries of the monthly values for various latitude bands (rows) of the following for all OSF scenarios of Table 2: The panels in the left column show the monthly median ($q_{0.5}$) of the XCO_2 noise error. The panels in the right column illustrate the number of data that are left after filtering for saturation in the pre-processing and after post-processing, i.e. data that have converged and are not filtered out during post-processing. In the latitude band between 60 and $90°$S, data coverage is small so that it is not shown here.

We also analyzed the monthly evolution of the error and the number of spectral samples for all OSF scenarios after post-processing, see Fig. 7. Timeseries of the global monthly median XCO_2 noise error for all OSF scenarios can be found in panel a. The noise increases by a constant factor between scenarios OSF 222, 232 and 333. This is different for OSF 111 because

330   the number of data (panel b) is decreased by about 20% in this scenario due to the saturation filtering. The noise error shows a semi-annual cycle with maximum values in June and December, the respective summer months on the hemispheres. These peaks can be seen in the individual latitude bands shown in the rows of Fig. 7. In addition, most of the data loss in the OSF 111 scenario occurs in latitudes between $40°S$ and $40°N$ where most of the deserts are located, consistent with the previous findings. As the SNR is connected to the noise error (see Fig. 4) and the signal over deserts is usually larger than the average,

335   the median noise error increases when the saturated spectra of desert regions are filtered out, which explains the anomalies in the noise error globally and in the near-tropical latitude bands (panels a, g and i). In all other latitudes, the median XCO_2 noise error increases with increased OSF in the SWIR bands, which are sensitive to changes in CO_2. The results of the northern mid-latitudes in Fig. 7e are the best approximation of the VEG50 scenario which is based on typical mid-latitude vegetation conditions like albedos and a solar zenith angle of $50°$ and which defines the requirements for CO2M (ESA, 2020). Tests with

340   VEG50 (not shown) showed similar values of the XCO_2 noise as in the winter months of the panel: approx. $0.7\,ppm$ for OSF 111, $0.77\,ppm$ for OSF 222 and about $0.88\,ppm$ for OSF 333. Therefore, these results are consistent with this experiment.

    As calculations of emissions depend linearly on the XCO_2 enhancement to some background value (e.g., Fuentes Andrade et al., 2024), the error of emission estimates scales linearly with the XCO_2 a posteriori noise of single soundings. Thus, the relative change in XCO_2 a posteriori noise is the same for uncertainties in the emissions. This was tested with a simple emission

345   model in the scope of this study. As an example, using mid-latitude summer conditions where the median XCO_2 a posteriori noise error increases from $0.45\,ppm$ (OSF 111) to $0.5\,ppm$ (OSF 222), see panel e of Fig. 7 in June, it can be expected that the relative increase in the uncertainty of the emission due to noise is the same: 1.11 in the median which can be larger for individual emission estimates.

    For the estimation of emissions, high precision of the measurements is needed which decreases with larger OSF. Therefore,

350   the columns of Fig. 8 show the fraction of post-processed data that are affected by a precision threshold of $0.7\,ppm$ and $1\,ppm$. This mostly affects the Northern mid and high latitudes. Most of the post-processed data have an a posteriori noise error smaller than $1\,ppm$. The global fraction of affected spatial samples is smaller than 3.2% for all OSF scenarios and is largest on Greenland where no significant sources of CO_2 exist. Furthermore, the possibility of glint mode could change these results especially over the snow-covered regions on Earth because snow has generally an enhanced forward scattering component

355   (e.g., Mikkonen et al., 2024). On the other hand, 6% of the post-processed data have a noise error larger than $0.7\,ppm$ in OSF 111, about 9% in the OSF scenario 222, more than 11% in OSF 232 and about 16% in OSF 333. Hence, estimates of emissions over Scandinavia, Canada and Northern Russia might be difficult when using an OSF larger than 2 because of the precision degradation there.

    In summary, these results imply that increasing the OSF globally to values larger than one leads to minor decreases in the

360   global median precision while increasing the coverage. Based on the simulated one-year subset of radiance data used here, the scenarios 111 and 222 seem to be favorable for CO2M in the future: Although OSF 111 will lead to saturation over the deserts and some snow-covered regions, the precision impact is smallest among the scenarios which might be of importance for the mid-latitudes. With the OSF scenario 222, we found nearly global coverage with respect to saturation, but a larger impact on the precision in the mid and high latitudes.
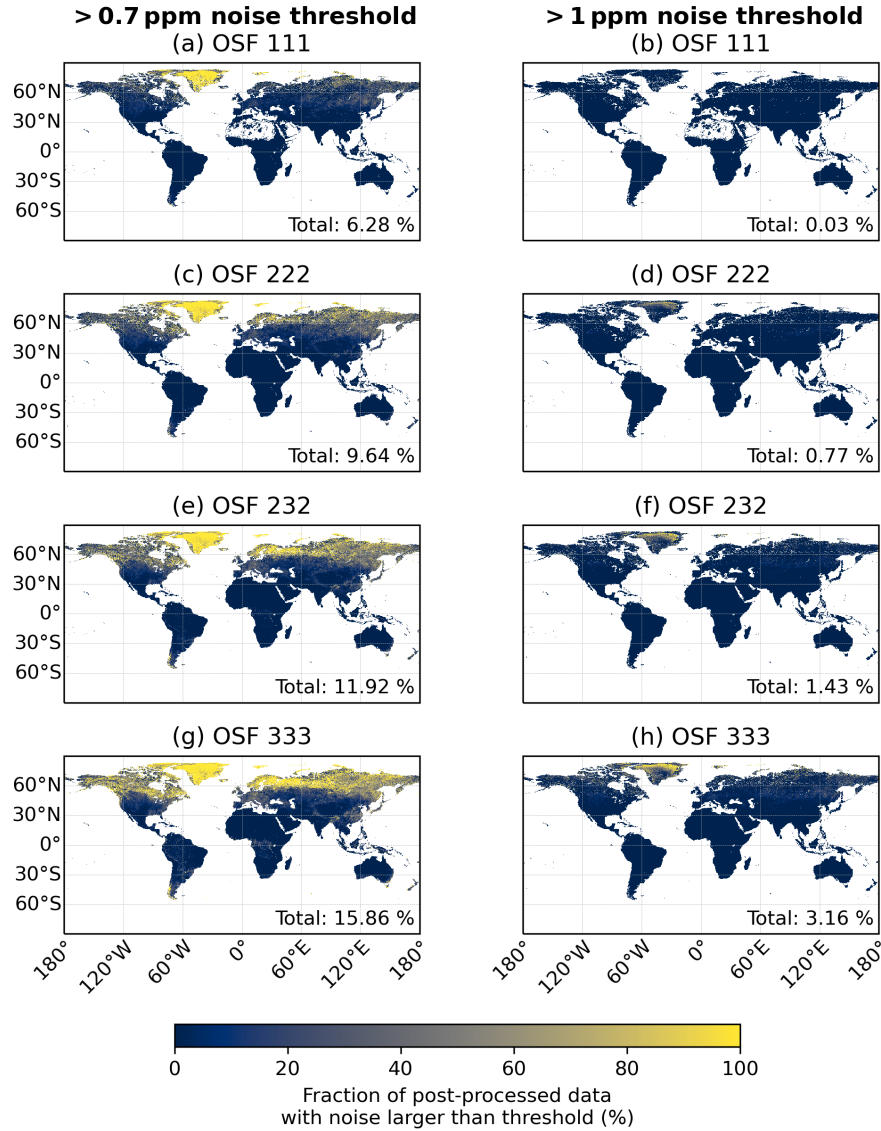
Figure 8. Fraction of spatial samples whose XCO_2 a posteriori noise error is larger than $0.7\,\mathrm{ppm}$ (left column), based on the precision requirement in ESA (2020), and $1\,\mathrm{ppm}$ (right column). The data are binned to a 0.4x0.4-degree latitude-longitude grid based on the CO2M spatial sample center coordinates. Note that the fraction is related to the data after postprocessing in this figure. The global fraction is labeled as "Total" in the panels.

7 Summary and Conclusions

The Copernicus Anthropogenic CO_2 Monitoring (CO2M) mission is a satellite constellation with the first satellite expected to be launched in ~~2026.~~ 2027. One of the operational greenhouse gas retrieval algorithms for CO2M will be the Fast atmOspheric

traCe gAs retrievaL (FOCAL) algorithm. In this study, we analyzed the impact of scenarios avoiding saturation of the detector which may occur for instance at bright scenes on the Earth's surface and which have to be filtered out during the retrieval so that the coverage is decreased. This can be avoided by increasing the number of read-outs per integration time step, i.e. increasing the oversampling factor (OSF) which, on the other hand, decreases the SNR of the measurement. We used idealized simulated radiances for this study with the goal being to investigate the long-term impact of using different OSFs. This was done by examining spatial-sample-wise saturation without considering any effect from either nearby bright scenes from the surrounding spatial samples or from nearby bright scenes outside the swath that could lead to saturation as well, such as stray light from nearby clouds. Clouds can lead to saturation as well so that the OSF might have to be increased for that scene.

We used a one-year subset dataset of simulated radiances for conditions of 2015 to define scenarios of OSFs and then to investigate the impact on XCO_2 using FOCAL. The post-processing was adapted depending on the used OSF because changing the OSF changes the retrieval-related detector properties. Our assumption was to keep one OSF setting for the whole globe and year to avoid possible calibration difficulties due to changing OSFs during the operation and to keep the operation of the satellite as simple as possible.

We compared the maximum radiances with the OSF-specific maximum radiance that can be detected in all spectral bands in order to define scenarios of OSFs to be used in the long-term analysis. We found that saturation especially occurs over deserts and the parts covered by rocks. Scenarios increasing the OSF for all CO2M spatial samples to values between two and three in the near-infrared (NIR) and short-wave infrared (SWIR) bands were defined which were called OSF 111 (baseline), 222, 232 and 333 in the order of OSFs set in the NIR, SWIR1 and SWIR2 bands, respectively.

We found that the decrease in signal-to-noise ratio (SNR) due to different OSFs has a wavelength-band-dependent impact on the XCO_2 a posteriori noise error, with smallest sensitivity in the SWIR2 band. The impact on XCO_2 was analyzed with distributions of the global noise error estimates which increased by a factor of 1.18 between OSF scenarios 111 and 333 and 1.06 between OSF 111 and 222, which in the median is not large but which leads to precision degradation in the Northern high-latitudes at the edge of emission estimation. The results showed that the filtered regions mostly include regions that are not known to have large emission sources. Therefore, the degradation of precision in these regions might be acceptable so that the assumption of a uniform OSF might also be relaxed and the OSF could be switched to OSF 222 over regions like the deserts and OSF 111 elsewhere.

This study used a fixed sampling period of $308\,\mathrm{ms}$ to meet the mission requirements. In principle, this value can be adjusted as well in order to get the optimum between SNR and saturation avoidance. Further investigations in the future could include the reduction of the sampling period instead of increasing the OSF. However, a smaller sampling period would further reduce the SNR and synchronization of the CO2I/NO2I spectrometers might become more difficult with a smaller sampling period.

The results of this study are based on idealized simulation of surface properties and assuming a perfect instrument. Thus, errors might be larger for real measurements and the results shown here can only provide a first insight towards the actual impact of changing the OSF when applied to real measurements. The analysis is limited to the nadir configuration over land and further investigations for other forseen geometries like ocean glint are needed in the future. In addition, the impact on emissions, especially in the northern high latitudes such as Scandinavia, Russia and Canada, should be further investigated in

more detail in the future. While the analysis of the saturation filtering is independent of the retrieval method used, the further results will depend on the retrieval algorithm and are likely to be different for Fusional-P-UOL-FP and RemoTAP. As discussed e.g. by Noël et al. (2024), the requirements concerning CH_4 are not as stringent as for CO_2 which is why we restricted the analysis to CO_2 in this study.

Overall, we found increases in the coverage when using OSFs larger than one and decreases in precision. Based on the idealized simulated radiances, the scenarios OSF 111 and 222 could be considered as possible OSF scenarios for CO2M for XCO_2 and under the assumption of a fixed OSF setting independent of the location. These results are intended to be used for the planning of the commissioning phase for CO2M.

Data availability. The data used in this study is available by the authors on request.

Appendix A: Retrieval setup for the OSF scenarios

As discussed in Sect. 5, the retrieval setup depends on the OSF scenario. For the forward model error, we strictly followed the concepts outlined by Reuter et al. (2017a) and Noël et al. (2024). Table A1 summarizes the variables used and the corresponding limits of the variance filter applied during post-processing.

Appendix B: Impact of removing whole swaths instead of single spatial samples

The analysis in this study assumes that neighboring spatial samples in the swath are not affected when saturation occurs. As the stray light correction is insufficient for the swath if saturation occurs in one spatial sample, there might be effects on neighboring spatial samples for CO2I/NO2I, which is why the analysis of saturation on the spatial coverage was also re-calculated with excluding whole swaths instead of single spatial samples, see Fig. B1.

As can be seen, the total fraction of left data for OSF111 is decreased significantly in comparison to Fig. 5 to about $47\,\%$ with similar global distribution and after postprocessing, the data left is reduced to $34.5\,\%$ for OSF 111. This is expected because additional data are removed at a similar location where saturation was identified in Fig. 5.

Apart from the total number of measurements, the results showed only minor changes in the order of $\pm 0.02\,\mathrm{ppm}$ in the XCO_2 precision.

Appendix C: Saturation and SNR for a range of sampling periods

As mentioned in Sect. 2, the selection of the sampling period t_{samp} is driven by CO2M mission requirements for spatial resolution and signal-to-noise ratios. In this appendix, we provide some more details about these requirements, add saturation to the discussion and generalize the analysis of saturation and SNR to different sampling periods.

Table A1. OSF-dependent limits of retrieval variables applied during post-processing to minimize the overall variance, sorted by their relevance. The variables are albedo coefficients $A_{i,band}$ of second-order polynomial and the cost function χ^2. No limit is denoted as dash. Note that the variable notation comes from Reuter et al. (2017a) and is not to be confused with the parameter A of the SNR in the main text.

OSF Scenario	Parameter	lower limit	upper limit
111	$A_{3,\mathrm{SWIR1}}$	$-2.5619 \cdot 10^{-5}$	–
	$A_{0,\mathrm{SWIR1}}$	0.1115	–
	$A_{3,\mathrm{SWIR2}}$	–	$3.6136 \cdot 10^{-5}$
	χ^2	–	1.0669
222	χ^2	–	1.0568
	$A_{0,\mathrm{NIR}}$	0.1037	–
	$A_{0,\mathrm{SWIR1}}$	0.1100	–
	$A_{3,\mathrm{SWIR2}}$	–	$5.1109 \cdot 10^{-5}$
	$A_{2,\mathrm{SWIR1}}$	$-4.1952 \cdot 10^{-5}$	–
	$A_{2,\mathrm{SWIR2}}$	–	$3.5254 \cdot 10^{-5}$
232	$A_{2,\mathrm{SWIR1}}$	$-4.3646 \cdot 10^{-5}$	–
	$A_{2,\mathrm{SWIR2}}$	-0.0002	$3.1977 \cdot 10^{-5}$
	$A_{0,\mathrm{SWIR1}}$	0.1127	–
	χ^2	–	1.0282
333	$A_{2,\mathrm{SWIR1}}$	$-4.5681 \cdot 10^{-5}$	–
	$A_{0,\mathrm{SWIR1}}$	0.1090	–
	$A_{3,\mathrm{SWIR2}}$	–	$6.7002 \cdot 10^{-5}$
	χ^2	–	1.0026

430 The A and B values for calculation of the SNR are given for $t_{\mathrm{samp}} = 308\,\mathrm{ms}$ and three OSFs. As parts of B depend on the integration time (see Eq. (6)) and parts only depend on the OSF, these parts have to be extracted which is done by a linear regression of B in dependence of the OSF. Substituting $u = I_{\mathrm{dark}} + I_{\mathrm{Tb}}$ and $v = N_{\mathrm{RO}}^2 + N_{\mathrm{AD}}^2 + N_{\mathrm{VC}}^2$ in Eq. (6) yields:

$$B = u \cdot [t_{\mathrm{samp},308} - (\mathrm{OSF} \cdot t_{\mathrm{RO}})] + v \cdot \mathrm{OSF}. \tag{C1}$$

Here, the numbers in the indices indicate that the sampling period is constant (308 ms) in this equation, which will be varied
435 in the later part of this section. Rearranging for OSF as x values yields:

$$B = (v - u \cdot t_{\mathrm{RO}}) \cdot \mathrm{OSF} + u \cdot t_{\mathrm{samp},308}. \tag{C2}$$
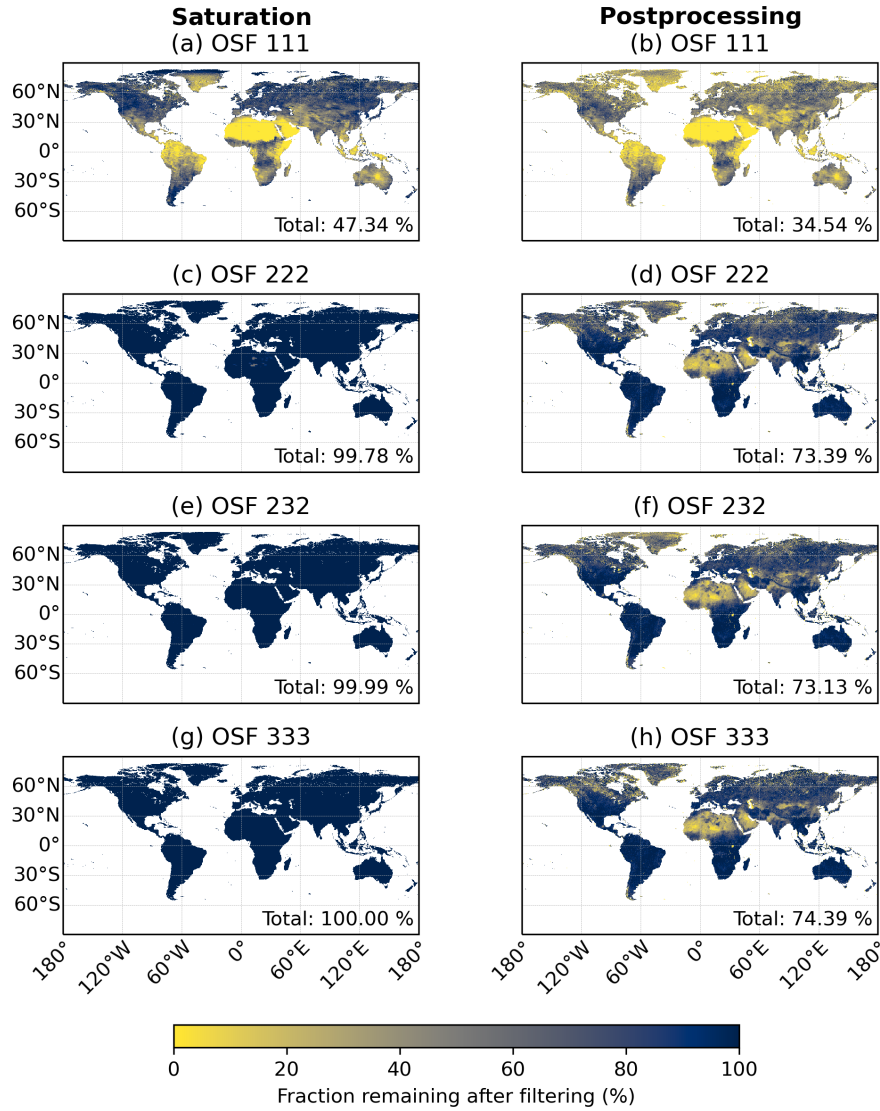
Figure B1. Same as left column of Fig. 5, but removing whole swaths instead of single spatial samples.

Linear regression with OSF on the x axis leads to a linear equation with slope m and intercept y_0, which can then be used to get the values for u:

$$u = \frac{y_0}{t_{\text{samp,308}}} \tag{C3}$$

and v

$$v = m + \frac{t_{\text{RO}} \, y_0}{t_{\text{samp,308}}} \tag{C4}$$
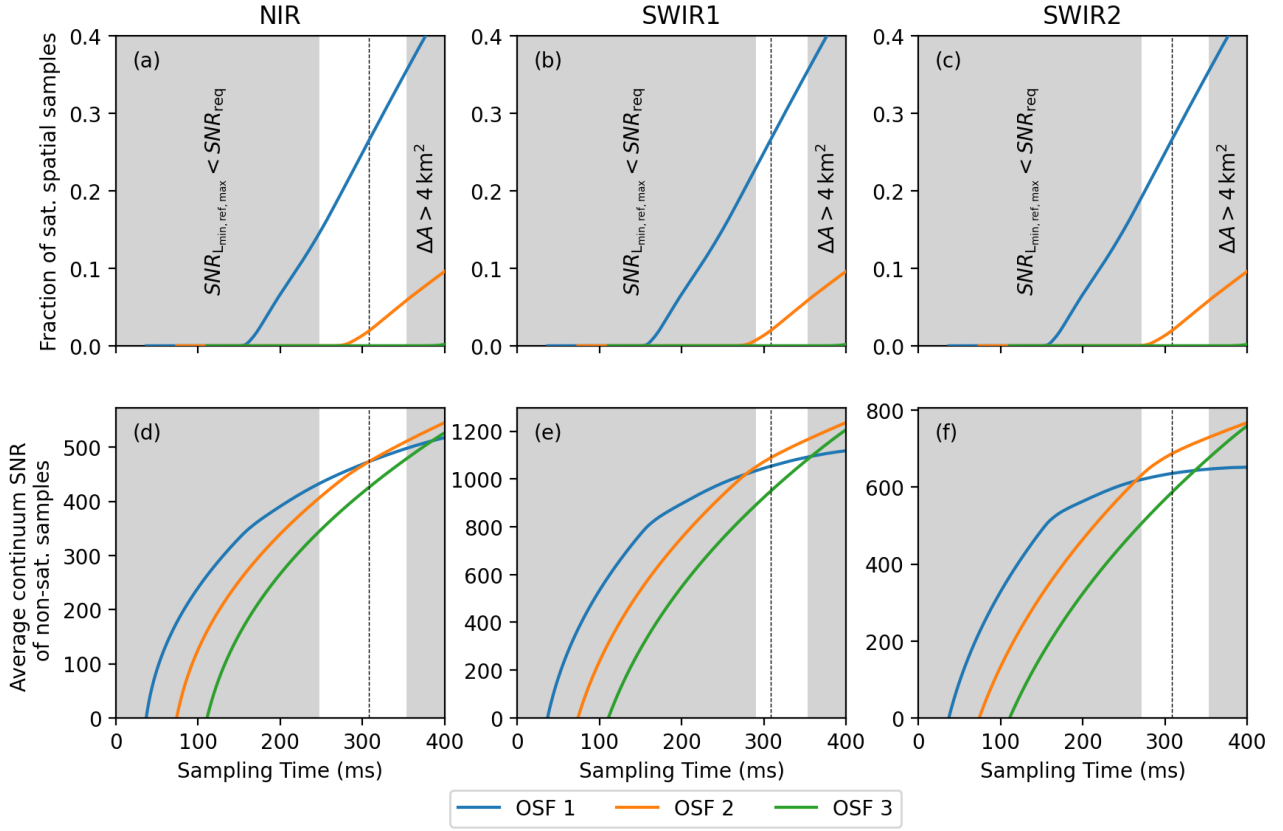
Figure C1. Saturation and SNR impact for a range of sampling periods. Grey shaded regions: Non-compliant with SNR and spatial footprint area requirements. First row: fraction of saturated spatial samples in the global subset dataset for OSF 1-3 in the (a) NIR, (b) SWIR1 and (c) SWIR2 bands. Second row: Global average of the spectral maximum SNR of non-saturated spatial samples for OSF 1-3 in the (d) NIR, (e) SWIR1 and (f) SWIR2 bands. The dashed vertical line depicts the sampling time of $308\,\mathrm{ms}$ that is used in the main text.

for each detector pixel. With these equations, the B values can be calculated for all possible sampling periods. For A, the given values have to be divided by the integration time, cf. Eq. (5), where we use the values of OSF 1 and the integration time of $271\,\mathrm{ms}$.

445   We first derive the sampling periods that are within the mission requirements of CO2M. The SNR requirement is given in ESA (2020) for specific radiance values $L_{\min}$, L_{ref} and $L_{\max}$ in each wavelength band. We calculate the SNR using A and B for sampling periods between 0 and $400\,\mathrm{ms}$ and the radiance values from ESA (2020) using OSF 1. Note that we neglect the issue that changes of the sampling period will also change the size of the footprints. The sampling period where the SNR for all radiances is smaller than the required SNR, $\mathrm{SNR}_{\mathrm{req}}$, is the minimum value for the sampling period, see left grey shaded

450   region in the panels of Fig. C1. As shown in this figure, the sampling period has to be larger than about $295\,\mathrm{ms}$ to be compliant with the SNR requirements of CO2M in all wavelength bands.

On the other hand, the sampling period has an upper limit because of the requirement of footprint area smaller than $4\,\mathrm{km}^2$ as described in the main text. Using the ground speed of the satellite of $7\,\mathrm{km/s}$, the ACT footprint width of $1.8\,\mathrm{km}$, and considering that during the read-out time t_RO no signal is measured (cf. Fig. 1), we arrive at a sampling period of about 350 ms, which is the maximum to be used to be compliant with the spatial extent of a CO2M footprint (right grey shaded region in the panels of Fig. C1).

Saturation (first row of Fig. C1) is evaluated for the complete 1-year subset dataset for all sampling periods and OSF scenarios. The fraction of spatial samples affected by saturation at one wavelength at least starts to increase from zero at $t_\mathrm{samp} \approx 150\,\mathrm{ms}$ for OSF 111 and increases with larger sampling periods. For OSF 222, the fraction starts to increase around $t_\mathrm{samp} \approx 290\,\mathrm{ms}$ with a slope that is smaller than for OSF 111. No saturation can be found for OSF 333 in the shown range of sampling periods between 0 and $400\,\mathrm{ms}$. The fractions at $t_\mathrm{samp} = 308\,\mathrm{ms}$ (black dashed line) are consistent with the results from Table 1.

As a final step, we take all non-saturated spatial samples of the subset dataset and calculate their maximum SNR for all sampling periods, which corresponds to the SNR in the continuum range of the spectra in the respective wavelength band. The global average of all non-saturated spatial samples is shown in the second row of Fig. C1. Note that this analysis is different from Fig. 3, where only spatial samples were analyzed where no saturation occurred in any OSF scenario. The SNR increases for larger sampling periods. The SNR can only be calculated if $\mathrm{OSF} \cdot t_\mathrm{RO} > t_\mathrm{samp}$, see Eq. (5). Since the SNR for saturated spectra cannot be calculated, but the spectra with saturation usually have the largest SNR, the average continuum SNR is decreased when filtering for saturation compared to non-filtered SNR. Hence, the global average SNR for OSF 1 becomes smaller than for OSF 2 between about $t_\mathrm{samp} = 290\,\mathrm{ms}$ and $t_\mathrm{samp} = 310\,\mathrm{ms}$, depending on the wavelength band, confirming the main result of this study, that OSF 222 is a possible scenario for CO2M in the future.

In the requirements-compliant range of sampling periods (white background in the panels of Fig. C1), the increase of the SNR is small and saturation should be avoided in general, so that a sampling period as small as possible should be used. Therefore, a sampling period close to the minimum in the requirements-compliant region was chosen and is set to $t_\mathrm{samp} = 308\,\mathrm{ms}$.

Author contributions. MW carried out the analysis and wrote the initial draft of the manuscript. YM provided the data about the oversampling setup. SN, MR and MH generated the one-year subset dataset of simulated radiances for this study. All authors contributed to write the manuscript.

Competing interests. The authors declare that they have no competing interests.

480 *Acknowledgements.* We acknowledge funding by the ESA CO2M Science Study under contract no. 4000138164/22/NL/SD, lead by SRON Netherlands Institute for Space Research. Parts of this work have been carried out with funding by the European Union Copernicus programme through EUMETSAT contract EUM/CO/19/4600002372/RL. Parts of this work are funded by the German Federal Ministry of Education and Research (BMBF) project "Integrated Greenhouse Gas Monitoring System for Germany – Observations (ITMS B)" under grant number 01 LK2103A and the State and the University of Bremen. All calculations reported here were performed on HPC facilities of
485 the IUP, University of Bremen, funded under DFG/FUGG grant INST 144/379-1 and INST 144/493-1.

References

Archer, D., Eby, M., Brovkin, V., Ridgwell, A., Cao, L., Mikolajewicz, U., Caldeira, K., Matsumoto, K., Munhoven, G., Montenegro, A., and Tokos, K.: Atmospheric Lifetime of Fossil Fuel Carbon Dioxide, Annu. Rev. Earth Pl. Sc., 37, 117–134, https://doi.org/10.1146/annurev.earth.031208.100206, 2009.

490 Boesch, H., Baker, D., Connor, B., Crisp, D., and Miller, C.: Global Characterization of CO2 Column Retrievals from Shortwave-Infrared Satellite Observations of the Orbiting Carbon Observatory-2 Mission, Remote Sens., 3, 270–304, https://doi.org/10.3390/rs3020270, 2011.

Bovensmann, H., Burrows, J. P., Buchwitz, M., Frerick, J., Noël, S., Rozanov, V. V., Chance, K. V., and Goede, A. P. H.: SCIA-MACHY: Mission Objectives and Measurement Modes, J. Atmos. Sci., 56, 127 – 150, https://doi.org/https://doi.org/10.1175/1520-0469(1999)056<0127:SMOAMM>2.0.CO;2, 1999.

495 Bovensmann, H., Buchwitz, M., Burrows, J. P., Reuter, M., Krings, T., Gerilowski, K., Schneising, O., Heymann, J., Tretner, A., and Erzinger, J.: A remote sensing technique for global monitoring of power plant CO_2 emissions from space and related applications, Atmos. Meas. Tech., 3, 781–811, https://doi.org/10.5194/amt-3-781-2010, 2010.

Broquet, G., Bréon, F.-M., Renault, E., Buchwitz, M., Reuter, M., Bovensmann, H., Chevallier, F., Wu, L., and Ciais, P.: The potential of satellite spectro-imagery for monitoring CO_2 emissions from large cities, Atmos. Meas. Tech., 11, 681–708, https://doi.org/10.5194/amt-500   11-681-2018, 2018.

Buchwitz, M., de Beek, R., Burrows, J. P., Bovensmann, H., Warneke, T., Notholt, J., Meirink, J. F., Goede, A. P. H., Bergamaschi, P., Körner, S., Heimann, M., and Schulz, A.: Atmospheric methane and carbon dioxide from SCIAMACHY satellite data: initial comparison with chemistry and transport models, Atmos. Chem. Phys., 5, 941–962, https://doi.org/10.5194/acp-5-941-2005, 2005.

Buchwitz, M., Reuter, M., Bovensmann, H., Pillai, D., Heymann, J., Schneising, O., Rozanov, V., Krings, T., Burrows, J. P., Boesch, H., 505   Gerbig, C., Meijer, Y., and Löscher, A.: Carbon Monitoring Satellite (CarbonSat): assessment of atmospheric CO_2 and CH_4 retrieval errors by error parameterization, Atmos. Meas. Tech., 6, 3477–3500, https://doi.org/10.5194/amt-6-3477-2013, 2013.

Burrows, J., Hölzle, E., Goede, A., Visser, H., and Fricke, W.: SCIAMACHY—scanning imaging absorption spectrometer for atmospheric chartography, Acta Astronaut., 35, 445–451, https://doi.org/https://doi.org/10.1016/0094-5765(94)00278-T, earth Observation, 1995.

Clavier, C., Meftah, M., Sarkissian, A., Romand, F., Hembise Fanton d'Andon, O., Mangin, A., Bekki, S., Dahoo, P.-R., Galopeau, P., 510   Lefèvre, F., Hauchecorne, A., and Keckhut, P.: Assessing Greenhouse Gas Monitoring Capabilities Using SolAtmos End-to-End Simulator: Application to the Uvsq-Sat NG Mission, Remote Sens., 16, https://doi.org/10.3390/rs16081442, 2024.

Cogan, A. J., Boesch, H., Parker, R. J., Feng, L., Palmer, P. I., Blavier, J.-F. L., Deutscher, N. M., Macatangay, R., Notholt, J., Roehl, C., Warneke, T., and Wunch, D.: Atmospheric carbon dioxide retrieved from the Greenhouse gases Observing SATellite (GOSAT): Comparison with ground-based TCCON observations and GEOS-Chem model calculations, J. Geophys. Res.: Atmospheres, 117, 515   https://doi.org/https://doi.org/10.1029/2012JD018087, 2012.

Copernicus Climate Change Service: Global Climate Highlights 2023, https://climate.copernicus.eu/global-climate-highlights-2023, last access 11 January 2024, 2024.

Crisp, D.: Measuring atmospheric carbon dioxide from space with the Orbiting Carbon Observatory-2 (OCO-2), in: Earth Observing Systems XX, edited by Butler, J. J., Xiong, X. J., and Gu, X., vol. 9607, p. 960702, International Society for Optics and Photonics, SPIE, 520   https://doi.org/10.1117/12.2187291, 2015.

Crisp, D., Pollock, H. R., Rosenberg, R., Chapsky, L., Lee, R. A. M., Oyafuso, F. A., Frankenberg, C., O'Dell, C. W., Bruegge, C. J., Doran, G. B., Eldering, A., Fisher, B. M., Fu, D., Gunson, M. R., Mandrake, L., Osterman, G. B., Schwandner, F. M., Sun, K., Taylor,

T. E., Wennberg, P. O., and Wunch, D.: The on-orbit performance of the Orbiting Carbon Observatory-2 (OCO-2) instrument and its radiometrically calibrated products, Atmos. Meas. Tech., 10, 59–81, https://doi.org/10.5194/amt-10-59-2017, 2017.

525 Eldering, A., Boland, S., Solish, B., Crisp, D., Kahn, P., and Gunson, M.: High precision atmospheric CO2 measurements from space: The design and implementation of OCO-2, in: 2012 IEEE Aerospace Conference, pp. 1–10, https://doi.org/10.1109/AERO.2012.6187176, 2012.

ESA: Copernicus CO2 Monitoring Mission Requirements Document, Tech. rep., ESA Earth and Mission Science Division, https://esamultimedia.esa.int/docs/EarthObservation/CO2M_MRD_v3.0_20201001_Issued.pdf, last access: 04 January 2024, 2020.

530 Fasnacht, L., Vogt, M.-L., Renard, P., and Brunner, P.: A 2D hyperspectral library of mineral reflectance, from 900 to 2500 nm, Sci. Data, 6, https://doi.org/10.1038/s41597-019-0261-9, 2019.

Forkel, M., Carvalhais, N., Rödenbeck, C., Keeling, R., Heimann, M., Thonicke, K., Zaehle, S., and Reichstein, M.: Enhanced seasonal CO2 exchange caused by amplified plant productivity in northern ecosystems, Science, 351, 696–699, https://doi.org/10.1126/science.aac4971, 2016.

535 Fuentes Andrade, B., Buchwitz, M., Reuter, M., Bovensmann, H., Richter, A., Boesch, H., and Burrows, J. P.: A method for estimating localized CO_2 emissions from co-located satellite XCO_2 and NO_2 images, Atmos. Meas. Tech., 17, 1145–1173, https://doi.org/10.5194/amt-17-1145-2024, 2024.

Gaucel, J.-M., Lefebure, A., Gaucher, A., Bouchage, G., and Sanson, E.: Remanence characterization of NGP detector in SWIR bands, in: International Conference on Space Optics — ICSO 2022, edited by Minoglou, K., Karafolas, N., and Cugny, B., vol. 12777, p. 127772E,
540 International Society for Optics and Photonics, SPIE, https://doi.org/10.1117/12.2689982, 2023.

Ge, Y., Atefi, A., Zhang, H., Miao, C., Ramamurthy, R. K., Sigmon, B., Yang, J., and Schnable, J. C.: High-throughput analysis of leaf physiological and chemical traits with VIS–NIR–SWIR spectroscopy: a case study with a maize diversity panel, Plant Methods, 15, 1746–4811, https://doi.org/10.1186/s13007-019-0450-8, 2019.

Grossmann, K., Frankenberg, C., Magney, T. S., Hurlock, S. C., Seibt, U., and Stutz, J.: PhotoSpec: A new instrument to
545 measure spatially distributed red and far-red Solar-Induced Chlorophyll Fluorescence, Remote Sens. Environ., 216, 311–327, https://doi.org/https://doi.org/10.1016/j.rse.2018.07.002, 2018.

Hersbach, H., Bell, B., Berrisford, P., Hirahara, S., Horányi, A., Muñoz Sabater, J., Nicolas, J., Peubey, C., Radu, R., Schepers, D., Simmons, A., Soci, C., Abdalla, S., Abellan, X., Balsamo, G., Bechtold, P., Biavati, G., Bidlot, J., Bonavita, M., De Chiara, G., Dahlgren, P., Dee, D., Diamantakis, M., Dragani, R., Flemming, J., Forbes, R., Fuentes, M., Geer, A., Haimberger, L., Healy, S., Hogan, R. J., Hólm, E.,
550 Janisková, M., Keeley, S., Laloyaux, P., Lopez, P., Lupu, C., Radnoti, G., de Rosnay, P., Rozum, I., Vamborg, F., Villaume, S., and Thépaut, J.-N.: The ERA5 global reanalysis, Q. J. Roy. Meteor. Soc., 146, 1999–2049, https://doi.org/https://doi.org/10.1002/qj.3803, 2020.

Inness, A., Ades, M., Agustí-Panareda, A., Barré, J., Benedictow, A., Blechschmidt, A.-M., Dominguez, J. J., Engelen, R., Eskes, H., Flemming, J., Huijnen, V., Jones, L., Kipling, Z., Massart, S., Parrington, M., Peuch, V.-H., Razinger, M., Remy, S., Schulz, M., and Suttie, M.: The CAMS reanalysis of atmospheric composition, Atmos. Chem. Phys., 19, 3515–3556, https://doi.org/10.5194/acp-19-3515-2019,
555 2019.

IPCC: Climate Change 2021 – The Physical Science Basis: Working Group I Contribution to the Sixth Assessment Report of the Intergovernmental Panel on Climate Change, Cambridge University Press, Cambridge, https://doi.org/10.1017/9781009157896, 2023.

Janssens-Maenhout, G., Pinty, B., Dowell, M., Zunker, H., Andersson, E., Balsamo, G., Bézy, J.-L., Brunhes, T., Bösch, H., Bojkov, B., Brunner, D., Buchwitz, M., Crisp, D., Ciais, P., Counet, P., Dee, D., van der Gon, H. D., Dolman, H., Drinkwater, M. R., Dubovik, O.,
560 Engelen, R., Fehr, T., Fernandez, V., Heimann, M., Holmlund, K., Houweling, S., Husband, R., Juvyns, O., Kentarchos, A., Landgraf, J.,

Lang, R., Löscher, A., Marshall, J., Meijer, Y., Nakajima, M., Palmer, P. I., Peylin, P., Rayner, P., Scholze, M., Sierk, B., Tamminen, J., and Veefkind, P.: Toward an Operational Anthropogenic CO2 Emissions Monitoring and Verification Support Capacity, B. Am. Meteorol. Soc., 101, E1439 – E1451, https://doi.org/https://doi.org/10.1175/BAMS-D-19-0017.1, 2020.

565 Kataoka, F., Crisp, D., Taylor, T. E., O'Dell, C. W., Kuze, A., Shiomi, K., Suto, H., Bruegge, C., Schwandner, F. M., Rosenberg, R., Chapsky, L., and Lee, R. A. M.: The Cross-Calibration of Spectral Radiances and Cross-Validation of CO2 Estimates from GOSAT and OCO-2, Remote Sens., 9, https://doi.org/10.3390/rs9111158, 2017.

Kuhlmann, G., Brunner, D., Broquet, G., and Meijer, Y.: Quantifying CO_2 emissions of a city with the Copernicus Anthropogenic CO_2 Monitoring satellite mission, Atmos. Meas. Tech., 13, 6733–6754, https://doi.org/10.5194/amt-13-6733-2020, 2020.

Kuze, A., Suto, H., Nakajima, M., and Hamazaki, T.: Thermal and near infrared sensor for carbon observation Fourier-transform
570 spectrometer on the Greenhouse Gases Observing Satellite for greenhouse gases monitoring, Appl. Opt., 48, 6716–6733, https://doi.org/10.1364/AO.48.006716, 2009.

Liu, Y., Wang, J., Yao, L., Chen, X., Cai, Z., Yang, D., Yin, Z., Gu, S., Tian, L., Lu, N., and Lyu, D.: The TanSat mission: preliminary global observations, Sci. Bull., 63, 1200–1207, https://doi.org/https://doi.org/10.1016/j.scib.2018.08.004, 2018.

Lu, S., Landgraf, J., Fu, G., van Diedenhoven, B., Wu, L., Rusli, S. P., and Hasekamp, O. P.: Simultaneous Retrieval of Trace Gases,
575 Aerosols, and Cirrus Using RemoTAP—The Global Orbit Ensemble Study for the CO2M Mission, Frontiers in Remote Sensing, 3, https://doi.org/10.3389/frsen.2022.914378, 2022.

Manakkakudy, A., Iacovo, A. D., Maiorana, E., Mitri, F., and Colace, L.: Material classification based on a SWIR discrete spectroscopy approach, Appl. Opt., 62, 9228–9237, https://doi.org/10.1364/AO.501582, 2023.

Meijer, Y., Andersson, E., Boesch, H., Dubovik, O., Houweling, S., Landgraf, J., Lang, R., and Lindqvist, H.: Edito-
580 rial: Anthropogenic emission monitoring with the Copernicus CO2 monitoring mission, Frontiers in Remote Sensing, 4, https://doi.org/10.3389/frsen.2023.1217568, 2023.

Mikkonen, A., Lindqvist, H., Peltoniemi, J., and Tamminen, J.: Non-Lambertian snow surface reflection models for simulated top-of-the-atmosphere radiances in the NIR and SWIR wavelengths, J. Quant. Spectrosc. Ra., 315, 108 892, https://doi.org/https://doi.org/10.1016/j.jqsrt.2023.108892, 2024.

585 Nakajima, M., Kuze, A., and Suto, H.: The current status of GOSAT and the concept of GOSAT-2, in: Sensors, Systems, and Next-Generation Satellites XVI, edited by Meynart, R., Neeck, S. P., and Shimoda, H., vol. 8533, p. 853306, International Society for Optics and Photonics, SPIE, https://doi.org/10.1117/12.974954, 2012.

Nakajima, M., Suto, H., Kuze, A., and Shiomi, K.: Optical Payloads onboard Japanese Greenhouse Gases Observing Satellite, chap. 21, pp. 459–499, John Wiley & Sons, Ltd, ISBN 9781118945179, https://doi.org/https://doi.org/10.1002/9781118945179.ch21, 2015.

590 Noël, S., Reuter, M., Buchwitz, M., Borchardt, J., Hilker, M., Bovensmann, H., Burrows, J. P., Di Noia, A., Suto, H., Yoshida, Y., Buschmann, M., Deutscher, N. M., Feist, D. G., Griffith, D. W. T., Hase, F., Kivi, R., Morino, I., Notholt, J., Ohyama, H., Petri, C., Podolske, J. R., Pollard, D. F., Sha, M. K., Shiomi, K., Sussmann, R., Té, Y., Velazco, V. A., and Warneke, T.: XCO_2 retrieval for GOSAT and GOSAT-2 based on the FOCAL algorithm, Atmos. Meas. Tech., 14, 3837–3869, https://doi.org/10.5194/amt-14-3837-2021, 2021.

Noël, S., Reuter, M., Buchwitz, M., Borchardt, J., Hilker, M., Schneising, O., Bovensmann, H., Burrows, J. P., Di Noia, A., Parker, R. J.,
595 Suto, H., Yoshida, Y., Buschmann, M., Deutscher, N. M., Feist, D. G., Griffith, D. W. T., Hase, F., Kivi, R., Liu, C., Morino, I., Notholt, J., Oh, Y.-S., Ohyama, H., Petri, C., Pollard, D. F., Rettinger, M., Roehl, C., Rousogenous, C., Sha, M. K., Shiomi, K., Strong, K., Sussmann, R., Té, Y., Velazco, V. A., Vrekoussis, M., and Warneke, T.: Retrieval of greenhouse gases from GOSAT and GOSAT-2 using the FOCAL algorithm, Atmos. Meas. Tech., 15, 3401–3437, https://doi.org/10.5194/amt-15-3401-2022, 2022.

Noël, S., Buchwitz, M., Hilker, M., Reuter, M., Weimer, M., Bovensmann, H., Burrows, J. P., Bösch, H., and Lang, R.: Greenhouse gas retrievals for the CO2M mission using the FOCAL method: first performance estimates, Atmos. Meas. Tech., 17, 2317–2334, https://doi.org/10.5194/amt-17-2317-2024, 2024.

Pillai, D., Buchwitz, M., Gerbig, C., Koch, T., Reuter, M., Bovensmann, H., Marshall, J., and Burrows, J. P.: Tracking city CO_2 emissions from space using a high-resolution inverse modelling approach: a case study for Berlin, Germany, Atmospheric Chemistry and Physics, 16, 9591–9610, https://doi.org/10.5194/acp-16-9591-2016, 2016.

Rascher, U., Agati, G., Alonso, L., Cecchi, G., Champagne, S., Colombo, R., Damm, A., Daumard, F., de Miguel, E., Fernandez, G., Franch, B., Franke, J., Gerbig, C., Gioli, B., Gómez, J. A., Goulas, Y., Guanter, L., Gutiérrez-de-la Cámara, O., Hamdi, K., Hostert, P., Jiménez, M., Kosvancova, M., Lognoli, D., Meroni, M., Miglietta, F., Moersch, A., Moreno, J., Moya, I., Neininger, B., Okujeni, A., Ounis, A., Palombi, L., Raimondi, V., Schickling, A., Sobrino, J. A., Stellmes, M., Toci, G., Toscano, P., Udelhoven, T., van der Linden, S., and Zaldei, A.: CEFLES2: the remote sensing component to quantify photosynthetic efficiency from the leaf to the region by measuring sun-induced fluorescence in the oxygen absorption bands, Biogeosciences, 6, 1181–1198, https://doi.org/10.5194/bg-6-1181-2009, 2009.

Reuter, M., Buchwitz, M., Schneising, O., Heymann, J., Bovensmann, H., and Burrows, J. P.: A method for improved SCIAMACHY CO_2 retrieval in the presence of optically thin clouds, Atmos. Meas. Tech., 3, 209–232, https://doi.org/10.5194/amt-3-209-2010, 2010.

Reuter, M., Bovensmann, H., Buchwitz, M., Burrows, J., Deutscher, N., Heymann, J., Rozanov, A., Schneising, O., Suto, H., Toon, G., and Warneke, T.: On the potential of the 2041–2047nm spectral region for remote sensing of atmospheric CO2 isotopologues, J. Quant. Spectrosc. Ra., 113, 2009–2017, https://doi.org/https://doi.org/10.1016/j.jqsrt.2012.07.013, 2012.

Reuter, M., Buchwitz, M., Schneising, O., Noël, S., Bovensmann, H., and Burrows, J. P.: A Fast Atmospheric Trace Gas Retrieval for Hyperspectral Instruments Approximating Multiple Scattering—Part 2: Application to XCO2 Retrievals from OCO-2, Remote Sens., 9, https://doi.org/10.3390/rs9111102, 2017a.

Reuter, M., Buchwitz, M., Schneising, O., Noël, S., Rozanov, V., Bovensmann, H., and Burrows, J. P.: A Fast Atmospheric Trace Gas Retrieval for Hyperspectral Instruments Approximating Multiple Scattering—Part 1: Radiative Transfer and a Potential OCO-2 XCO2 Retrieval Setup, Remote Sens., 9, https://doi.org/10.3390/rs9111159, 2017b.

Reuter, M., Buchwitz, M., Schneising, O., Krautwurst, S., O'Dell, C. W., Richter, A., Bovensmann, H., and Burrows, J. P.: Towards monitoring localized CO_2 emissions from space: co-located regional CO_2 and NO_2 enhancements observed by the OCO-2 and S5P satellites, Atmos. Chem. Phys., 19, 9371–9383, https://doi.org/10.5194/acp-19-9371-2019, 2019.

Reuter, M., Hilker, M., Noël, S., Di Noia, A., Weimer, M., Schneising, O., Buchwitz, M., Bovensmann, H., Burrows, J. P., Bösch, H., and Lang, R.: Retrieving the atmospheric concentrations of carbon dioxide and methane from the European Copernicus CO2M satellite mission using artificial neural networks, EGUsphere [preprint], 2024, 1–32, https://doi.org/10.5194/egusphere-2024-2365, 2024.

Rodgers, C. D.: Inverse Methods for Atmospheric Sounding, WORLD SCIENTIFIC, https://doi.org/10.1142/3171, 2000.

Rozanov, V., Dinter, T., Rozanov, A., Wolanin, A., Bracher, A., and Burrows, J.: Radiative transfer modeling through terrestrial atmosphere and ocean accounting for inelastic processes: Software package SCIATRAN, J. Quant. Spectrosc. Ra., 194, 65–85, https://doi.org/https://doi.org/10.1016/j.jqsrt.2017.03.009, 2017.

Santamaría-López, A., Suárez, M., and García-Romero, E.: Detection limits of kaolinites and some common minerals in binary mixtures by short-wave infrared spectroscopy, Appl. Clay Sci., 250, 107 269, https://doi.org/https://doi.org/10.1016/j.clay.2024.107269, 2024.

Schneising, O., Buchwitz, M., Reuter, M., Heymann, J., Bovensmann, H., and Burrows, J. P.: Long-term analysis of carbon dioxide and methane column-averaged mole fractions retrieved from SCIAMACHY, Atmos. Chem. Phys., 11, 2863–2880, https://doi.org/10.5194/acp-11-2863-2011, 2011.

Shi, H., Li, Z., Ye, H., Luo, H., Xiong, W., and Wang, X.: First Level 1 Product Results of the Greenhouse Gas Monitoring Instrument on the GaoFen-5 Satellite, IEEE T. Geosci. Remote, 59, 899–914, https://doi.org/10.1109/TGRS.2020.2998729, 2021.

Sierk, B., Fernandez, V., Bézy, J.-L., Meijer, Y., Durand, Y., Courrèges-Lacoste, G., Pachot, C., Löscher, A., Nett, H., Minoglou, K., Boucher, L., Windpassinger, R., Pasquet, A., Serre, D., and Hennepe, F.: The Copernicus CO2M mission for monitoring anthropogenic carbon dioxide emissions from space, in: Proc. SPIE, p. 128, https://doi.org/10.1117/12.2599613, 2021.

Solomon, S., Plattner, G.-K., Knutti, R., and Friedlingstein, P.: Irreversible climate change due to carbon dioxide emissions, P. Natl. A. Sci., 106, 1704–1709, https://doi.org/10.1073/pnas.0812721106, 2009.

Staebell, C., Sun, K., Samra, J., Franklin, J., Chan Miller, C., Liu, X., Conway, E., Chance, K., Milligan, S., and Wofsy, S.: Spectral calibration of the MethaneAIR instrument, Atmos. Meas. Tech., 14, 3737–3753, https://doi.org/10.5194/amt-14-3737-2021, 2021.

Taylor, T. E., Eldering, A., Merrelli, A., Kiel, M., Somkuti, P., Cheng, C., Rosenberg, R., Fisher, B., Crisp, D., Basilio, R., Bennett, M., Cervantes, D., Chang, A., Dang, L., Frankenberg, C., Haemmerle, V. R., Keller, G. R., Kurosu, T., Laughner, J. L., Lee, R., Marchetti, Y., Nelson, R. R., O'Dell, C. W., Osterman, G., Pavlick, R., Roehl, C., Schneider, R., Spiers, G., To, C., Wells, C., Wennberg, P. O., Yelamanchili, A., and Yu, S.: OCO-3 early mission operations and initial (vEarly) XCO2 and SIF retrievals, Remote Sens. Environ., 251, 112 032, https://doi.org/https://doi.org/10.1016/j.rse.2020.112032, 2020.

Taylor, T. E., O'Dell, C. W., Crisp, D., Kuze, A., Lindqvist, H., Wennberg, P. O., Chatterjee, A., Gunson, M., Eldering, A., Fisher, B., Kiel, M., Nelson, R. R., Merrelli, A., Osterman, G., Chevallier, F., Palmer, P. I., Feng, L., Deutscher, N. M., Dubey, M. K., Feist, D. G., García, O. E., Griffith, D. W. T., Hase, F., Iraci, L. T., Kivi, R., Liu, C., De Mazière, M., Morino, I., Notholt, J., Oh, Y.-S., Ohyama, H., Pollard, D. F., Rettinger, M., Schneider, M., Roehl, C. M., Sha, M. K., Shiomi, K., Strong, K., Sussmann, R., Té, Y., Velazco, V. A., Vrekoussis, M., Warneke, T., and Wunch, D.: An 11-year record of XCO_2 estimates derived from GOSAT measurements using the NASA ACOS version 9 retrieval algorithm, Earth Syst. Sci. Data, 14, 325–360, https://doi.org/10.5194/essd-14-325-2022, 2022.

Tian, Y., Sun, Y., Liu, C., Xie, P., Chan, K., Xu, J., Wang, W., and Liu, J.: Characterization of urban CO2 column abundance with a portable low resolution spectrometer (PLRS): Comparisons with GOSAT and GEOS-Chem model data, Sci. Total Environ., 612, 1593–1609, https://doi.org/https://doi.org/10.1016/j.scitotenv.2016.12.005, 2018.

UNFCCC: UNFCCC Paris Agreement, https://unfccc.int/sites/default/files/english_paris_agreement.pdf, last access: 21 December 2023, 2015.

Velazco, V. A., Buchwitz, M., Bovensmann, H., Reuter, M., Schneising, O., Heymann, J., Krings, T., Gerilowski, K., and Burrows, J. P.: Towards space based verification of CO_2 emissions from strong localized sources: fossil fuel power plant emissions as seen by a CarbonSat constellation, Atmos. Meas. Tech., 4, 2809–2822, https://doi.org/10.5194/amt-4-2809-2011, 2011.

Yoshida, Y., Ota, Y., Eguchi, N., Kikuchi, N., Nobuta, K., Tran, H., Morino, I., and Yokota, T.: Retrieval algorithm for CO_2 and CH_4 column abundances from short-wavelength infrared spectral observations by the Greenhouse gases observing satellite, Atmos. Meas. Tech., 4, 717–734, https://doi.org/10.5194/amt-4-717-2011, 2011.

Zeng, Y., Hao, D., Badgley, G., Damm, A., Rascher, U., Ryu, Y., Johnson, J., Krieger, V., Wu, S., Qiu, H., Liu, Y., Berry, J. A., and Chen, M.: Estimating near-infrared reflectance of vegetation from hyperspectral data, Remote Sens. Environ., 267, 112 723, https://doi.org/https://doi.org/10.1016/j.rse.2021.112723, 2021.